Article

Tracing the origin of hair follicle stem cells

https://doi.org/10.1038/s41586-021-03638-5

Received: 30 March 2020

Accepted: 13 May 2021

Published online: 9 June 2021

Check for updates

Ritsuko Morita[1], Noriko Sanzen[1], Hiroko Sasaki[1], Tetsutaro Hayashi[2], Mana Umeda[2], Mika Yoshimura[2], Takaki Yamamoto[3,4], Tatsuo Shibata[4], Takaya Abe[5], Hiroshi Kiyonari[5], Yasuhide Furuta[5,6], Itoshi Nikaido[2,7,8] & Hironobu Fujiwara[1]✉

Tissue stem cells are generated from a population of embryonic progenitors through organ-specific morphogenetic events[1,2]. Although tissue stem cells are central to organ homeostasis and regeneration, it remains unclear how they are induced during development, mainly because of the lack of markers that exclusively label prospective stem cells. Here we combine marker-independent long-term 3D live imaging and single-cell transcriptomics to capture a dynamic lineage progression and transcriptome changes in the entire epithelium of the mouse hair follicle as it develops. We found that the precursors of different epithelial lineages were aligned in a 2D concentric manner in the basal layer of the hair placode. Each concentric ring acquired unique transcriptomes and extended to form longitudinally aligned, 3D cylindrical compartments. Prospective bulge stem cells were derived from the peripheral ring of the placode basal layer, but not from suprabasal cells (as was previously suggested[3]). The fate of placode cells is determined by the cell position, rather than by the orientation of cell division. We also identified 13 gene clusters: the ensemble expression dynamics of these clusters drew the entire transcriptional landscape of epithelial lineage diversification, consistent with cell lineage data. Combining these findings with previous work on the development of appendages in insects[4,5], we describe the 'telescope model', a generalized model for the development of ectodermal organs in which 2D concentric zones in the placode telescope out to form 3D longitudinally aligned cylindrical compartments.

Most ectodermal appendages, including hair follicles, form from the placode[6]. The hair placode elongates towards the dermis and develops into a cylindrical structure with longitudinally aligned compartments, one of which is the SOX9$^+$ bulge stem cell compartment[7,8]. Previous studies have shown that SOX9$^+$ suprabasal cells generated by the asymmetric division of basal epithelial cells of the placode become bulge stem cells[1,3,9], which suggests that stem cells are first specified by asymmetric cell division. However, it remains unclear how the immature placode cells develop into the mature hair follicle structure and how organ-wide lineage diversification, including that of stem cells, is orchestrated at the cellular and transcriptional levels.

One major obstacle to studying the developmental origins of epithelial lineages is the lack of specific markers to enable the prospective identification and tracking of each cell lineage. Although basal epithelial cells in the whisker hair follicles of mice acquired the expression pattern of compartmentalized stem cell markers characteristic of mature hair follicles by embryonic day (E)17.0, the origin and early induction process of bulge stem cells could not be traced by the known adult stem cell markers SOX9, NFATc1, LHX2 or KRT15 because of wide spatiotemporal variation in expression of these markers[9–13] (Extended Data Fig. 1).

Stem cells are derived from placode outer ring

To investigate the developmental origin and lineage dynamics of hair follicle stem cells without relying on molecular markers, we developed a long-term ex vivo culture and imaging system of whisker hair follicles that enables the observation of organ-wide progression of cell lineages[14] (Extended Data Fig. 2a). Our cultured explants reflect in vivo hair follicle morphogenesis and lineage specification well (Extended Data Fig. 2b–d). Using embryonic whisker explants from transgenic mice expressing enhanced GFP-labelled histone 2B (H2B–eGFP) in the epithelium, we continuously imaged and tracked epithelial cells from the hair germ stage (E13.0) to the bulbous peg stage (E13.0 + 60 h) (Fig. 1a, Extended Data Fig. 3a–c). We colour-coded the reconstructed 3D cell trajectories according to their positions at the hair germ stage (Fig. 1a, Extended Data Fig. 3a, Supplementary Video 1). After 60 h of culture, most of the basal cells in the upper region of hair-germ-stage hair follicles (shown in red in Fig. 1a) generated basal cells in the upper region of bulbous-peg-stage hair follicles (that is, the SOX9$^+$NFATc1$^+$ low-proliferative prebulge region) (Extended Data Fig. 1), whereas the lower part (shown in yellow in Fig. 1a) contributed mainly to the lower region of bulbous-peg-stage hair follicles (Fig. 1a, b, Extended Data Fig. 3d–f, Supplementary Videos 1, 2). Cells adjacent to the dermal

[1]Laboratory for Tissue Microenvironment, RIKEN Center for Biosystems Dynamics Research, Kobe, Japan. [2]Laboratory for Bioinformatics Research, RIKEN Center for Biosystems Dynamics Research, Kobe, Japan. [3]Nonequilibrium Physics of Living Matter RIKEN Hakubi Research Team, RIKEN Center for Biosystems Dynamics Research, Kobe, Japan. [4]Laboratory for Physical Biology, RIKEN Center for Biosystems Dynamics Research, Kobe, Japan. [5]Laboratory for Animal Resources and Genetic Engineering, RIKEN Center for Biosystems Dynamics Research, Kobe, Japan. [6]Mouse Genetics Core Facility, Sloan Kettering Institute, Memorial Sloan Kettering Cancer Center, New York, NY, USA. [7]Master's and Doctoral Program in Life Science Innovation (Bioinformatics), Degree Programs in Systems and Information Engineering, Graduate School of Science and Technology, University of Tsukuba, Tsukuba, Japan. [8]Functional Genome Informatics, Medical Research Institute, Tokyo Medical and Dental University, Tokyo, Japan. ✉e-mail: hironobu.fujiwara@riken.jp

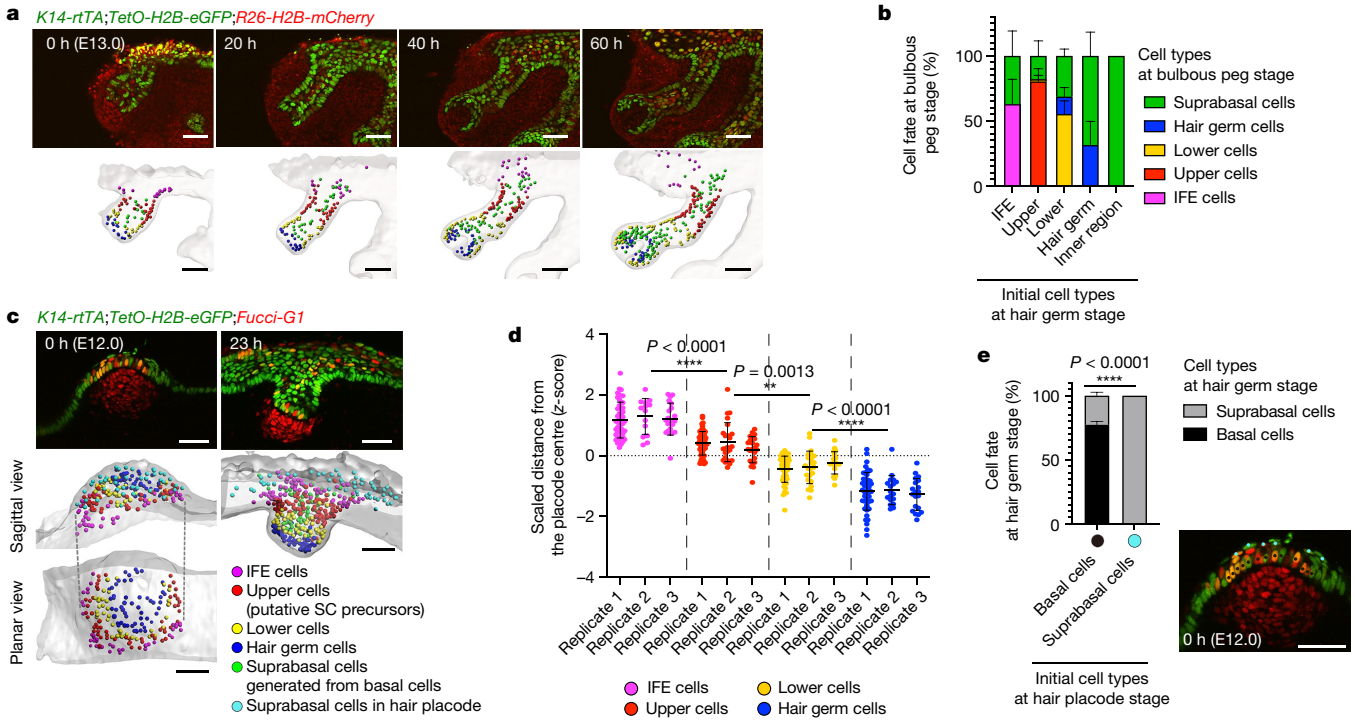

Fig. 1 | Bulge stem cells are derived from the periphery of the placode basal layer. a, Snapshots of the 3D time-lapse movie (top) and cell tracking data (bottom) of a developing whisker hair follicle from the hair germ to bulbous peg stages. Cells in the wire frames are colour-coded on the basis of their original positions at the hair germ stage. Scale bars, 100 µm. **b**, Fate of epithelial cells of the IFE, upper, lower, hair germ and inner regions of the whisker hair follicle at the hair germ stage. Cell fates at the bulbous peg stage are shown. **c**, Snapshot images (top) and lineage tracking data (bottom) of live imaging of the development of a whisker hair follicle from the hair placode to hair germ stages. SC, stem cell. Scale bars, 50 µm. **d**, Bee swarm plot showing the distances of cells from the placode centre. Different epithelial lineages are aligned in a concentric manner in the placode. Values were scaled on the basis of the diameter of each placode. Two-sided nested *t*-test was used. **e**, Fate of basal and suprabasal cells of the hair placode. Cell fates at the hair germ stage are shown. Two-sided Fisher's exact test was used. Black spots, tracked basal cells. Cyan spots, tracked suprabasal cells. Scale bar, 50 µm. The embryonic stage at which imaging started is indicated in each figure. Each value in the graph is mean ± s.d. from three independent experiments (one hair follicle each.) Extended Data Figure 3 contains further details and statistical tests. The numbers of analysed cell lineages are summarized in Supplementary Table 1; see Source Data and 'Statistical analysis and reproducibility' in Methods for further information on statistics.

papilla (shown in blue in Fig. 1a) (hair germ cells or matrix precursors) remained at the interface between the epithelium and the dermal papilla, or detached from the basement membrane and differentiated. Our data indicate that each longitudinally aligned compartment of the basal epithelium in the early-to-middle stages of hair follicle morphogenesis is induced by enlarging each of the early compartments, rather than being sequentially added by the cell supply from the leading hair germ (shown in blue in Fig. 1a) or other regions. Thus, prospective bulge stem cells are located in the upper region of hair-germ-stage hair follicles and mostly form the prebulge compartment, but do not substantially contribute to other basal compartments during morphogenesis.

To identify the origin and earlier lineage dynamics of hair follicle epithelial cells, we obtained live imaging data from the hair placode stage using *KRT14-rtTA* (hereafter *K14-rtTA*);*TetO-H2B-eGFP*;*Fucci-G1* mice (Supplementary Videos 2, 3). We performed retrospective cell tracking from the hair germ stage to the placode stage, which revealed that epithelial cells located adjacent to the dermal papilla (shown in blue in Fig. 1c) were originally located at the centre of the basal layer of the placode (Fig. 1c, d, Extended Data Fig. 3g, h, Supplementary Video 4). Cells in the lower region (shown in yellow in Fig. 1c) were derived from immediately outside the centre region of the placode shown in blue in Fig. 1c. Cells in the upper region (shown in red in Fig. 1c) (putative prospective bulge stem cells) were derived from the peripheral ring of the basal layer of the placode. Suprabasal cells located inside of the hair follicles (shown in green in Fig. 1c) were derived from both suprabasal and basal cells that abut the dermal condensate at the placode stage. Suprabasal cells with a flat nucleus at the placode stage (shown in cyan in Fig. 1c, e) (equivalent to SOX9$^+$ suprabasal cells in Extended Data Figs. 1a, b, 5e) did not contribute to the basal layer or hair follicle formation (Fig. 1c, e, Extended Data Fig. 3i, Supplementary Video 5).

Our results demonstrate that (1) the origin of the longitudinally aligned cylindrical compartments of the epithelium of the whisker hair follicle in three dimensions are mapped as 2D concentric rings in the basal layer of the placode, (2) only cells in the basal layer of the epithelium contribute to follicle formation, (3) prospective bulge stem cells are derived from epithelial basal cells in the placode periphery, (4) 3D epithelial cylindrical compartments are formed by enlarging each 2D concentric zone in the placode and (5) prospective bulge stem cells do not substantially contribute to forming other basal compartments during hair follicle morphogenesis (Extended Data Fig. 3j).

Position governs placode cell fate

It has previously been reported that the hair follicle stem cells of dorsal hair follicles are derived from SOX9$^+$WNT^{low} suprabasal cells that are generated by perpendicular and asymmetric cell divisions of placode basal cells[3]. To assess the relationship between the cell division orientation and later cell fate in the early development of whisker hair follicles, we measured the orientation of cell division against the basement membrane zone three-dimensionally in the basal layer of the epithelium across the placode and interfollicular epidermis (IFE) in our live imaging data (Extended Data Fig. 4). We categorized cells into horizontally and perpendicularly divided cell groups in each

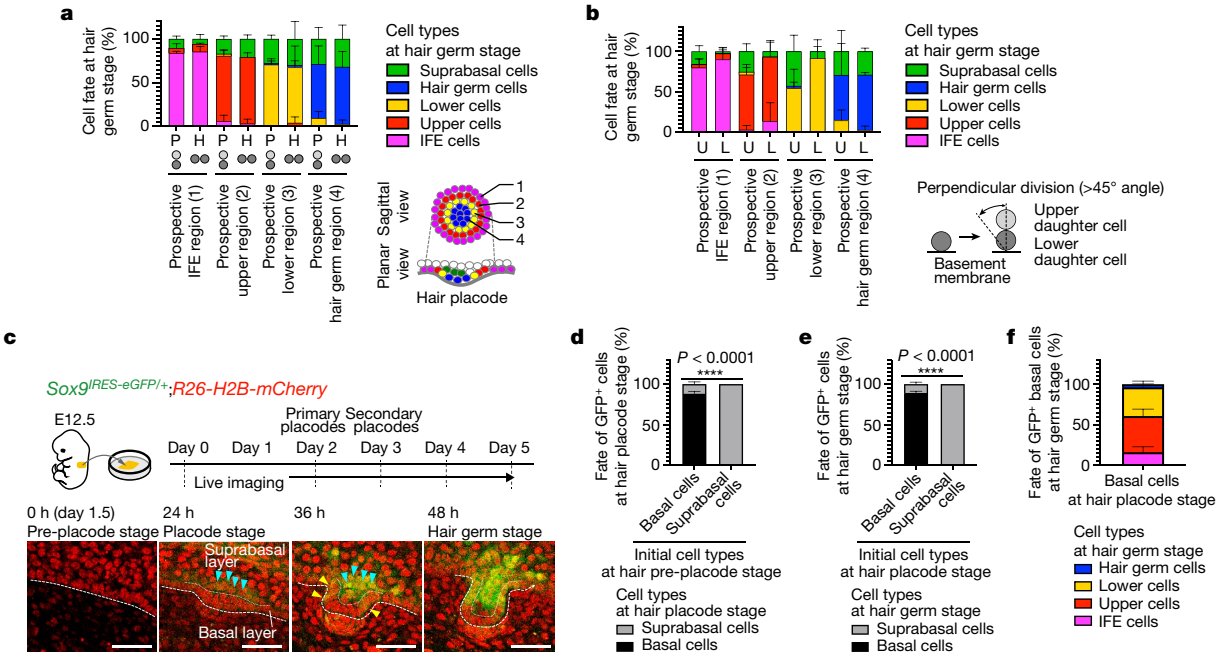

Fig. 2 | Cell fate determination relies on cell position. a, Fate of daughter cells generated by horizontal or perpendicular cell divisions in each region of the whisker hair placode. Cell fates at the hair germ stage are shown. H, daughter cells produced by horizontal division (<45° angle); P, daughter cells produced by perpendicular division (>45° angle). **b**, Fate of upper (U) and lower (L) daughter cells produced by perpendicular divisions in each region of the whisker hair placode. Cell fates at the hair germ stage are shown. **c**, Strategy for live imaging (top) and snapshot images (bottom) of ex-vivo-cultured dorsal hair follicles derived from E12.5 *Sox9*$^{IRES\text{-}eGFP/+}$;*R26-H2B-mCherry* mice (*Sox9-IRES-eGFP* reporter mice). GFP expression was detected in suprabasal cells (cyan arrowheads) and basal cells (yellow arrowheads). Scale bars, 50 µm. **d**, Fate of basal and suprabasal cells in pre-placodes of *Sox9-IRES-eGFP*-reporter-derived dorsal skin explants. Fates of GFP$^+$ cells at hair placode stage are shown. GFP$^+$ cell lineages were determined at hair germ stage. Two-sided Fisher's exact test was used. **e**, Fate of basal and suprabasal cells in placodes of *Sox9-IRES-eGFP*-reporter-derived dorsal skin explants. Fates of GFP$^+$ cells at the hair germ stage are shown. Two-sided Fisher's exact test was used. **f**, Lineage distribution of GFP$^+$ basal cells at hair germ stage. Cells grouped in the black bar in **e** were examined. The embryonic stage at which imaging started is indicated in each figure. Each value in the graph is mean ± s.d. from three independent experiments (one hair follicle each). Extended Data Figure 5 contains further details and statistical tests. The numbers of analysed cell lineages are summarized in Supplementary Table 2; see Source Data and 'Statistical analysis and reproducibility' in Methods for further information on statistics.

tissue region, and tracked the fates of their daughter cells up to the hair germ stage (Fig. 2a, b, Extended Data Fig. 5a, b). Irrespective of the angle of cell division, most daughter cells from the basal layer of the placode of prospective upper, lower and hair germ regions contributed to basal cells in upper, lower and hair germ regions of the hair germ stage, respectively (Fig. 2a). Moreover, both upper and lower daughter cells of perpendicular division in the prospective upper region contributed significantly (Extended Data Fig. 5b) to forming the prospective stem cell region as compared to other regions (shown in red in Fig. 2b). Throughout development, upper daughter cells produced by perpendicular division often remained in the basal layer and acquired a cell fate according to their position (Supplementary Video 6). Furthermore, upper daughter cells in the basal layer of the placode remained positive for LHX2, whereas SOX9$^+$ suprabasal cells were negative for LHX2 (Extended Data Fig. 5c). These observations suggest that upper daughter cells retain some—if not all—of the properties of basal cells immediately after cell division and are distinct from SOX9$^+$ suprabasal cells. Together, these results indicate that the fate of epithelial cells in the whisker placode is determined by the cell position within the placode, regardless of the orientation of cell division.

We next asked whether prospective bulge stem cells were derived from *Sox9*-expressing or SOX9$^+$ suprabasal cells in the placode. We first confirmed that there are two distinct SOX9$^+$ cell populations in the placodes of whisker and dorsal hair follicles (Extended Data Fig. 5d, e). As has previously been reported[3,9], suprabasal cells showed a high expression of SOX9. However, basal cells at the placode periphery also exhibited moderate expression of SOX9. We established a long-term explant ex vivo culture system using embryonic dorsal skin that recapitulates the formation of first- and second-wave hair follicles in vivo (Extended Data Fig. 5f–h, Supplementary Video 7, 8). We performed 4D tracking, which revealed that different lineages of hair follicle epithelial cells were mapped as 2D concentric rings in the basal layer of the placode—as we observed in whisker hair follicles (Extended Data Fig. 5i–l). We subsequently investigated the fate of *Sox9*-expressing cells using live imaging data of dorsal skin explants from *Sox9-IRES-eGFP;Rosa26* (hereafter *R26*)*-H2B-mCherry* mice. We detected eGFP signals first in the suprabasal layer of placodes, which was followed by expression at the periphery of the basal layer of the placode (Fig. 2c, Supplementary Video 8), consistent with the expression strength and pattern of SOX9 immunostaining results (Extended Data Fig. 5d). Our retrospective tracking of these *Sox9*- and eGFP-expressing cells confirmed that only cells initially located in the basal layer of pre-placodes and placodes contributed to the basal layer at the hair germ stage. These cells mainly gave rise to the upper cells at the hair germ stage (prospective bulge stem cells), whereas *Sox9*- and eGFP-expressing suprabasal cells did not contribute to the basal layer of the hair germ stage, including the upper cells (Fig. 2d–f, Extended Data Fig. 5m–o, Supplementary Video 5). We also performed live imaging with skin explants from *Sox9-creERt2;R26R-H2B-mCherry;K14-H2B-eGFP* mice. We induced *Sox9-creERt2*-mediated recombination at the hair placode stage, and retrospectively traced H2B–mCherry$^+$ cells from the hair germ stage to the placode stage (Extended Data Fig. 5p). As we observed in the *Sox9-IRES-eGFP* mouse experiments, H2B–mCherry$^+$ suprabasal cells did not contribute to the

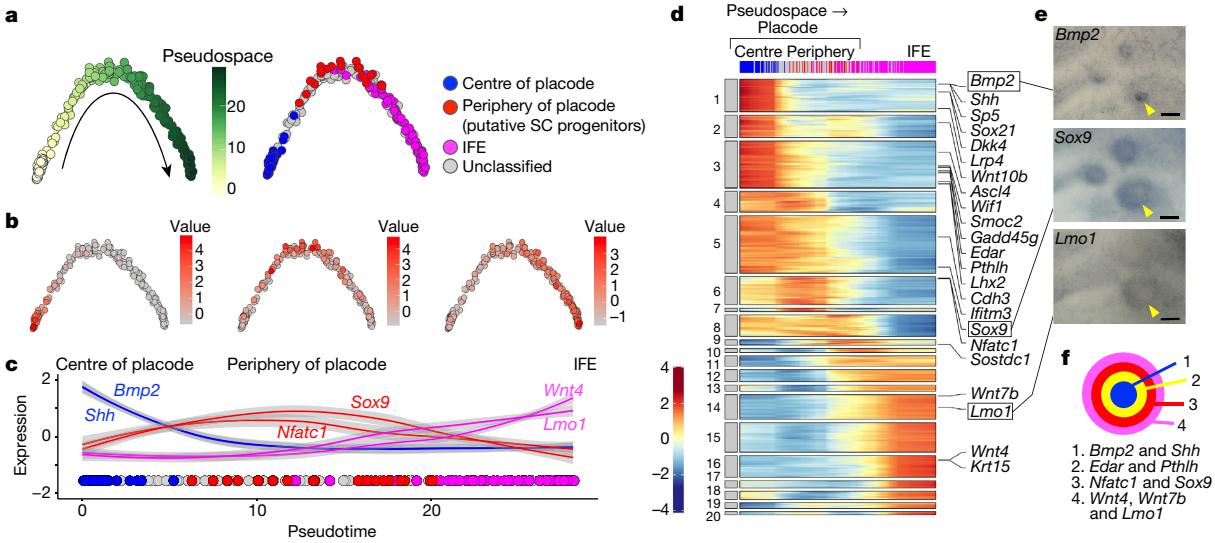

Fig. 3 | Two-dimensional concentric transcriptional landscape characterizes stem cell origin. a, Pseudospatial ordering of 270 epithelial cells derived from the E12.0 placode. Cells were classified by each lineage marker gene using the Monocle2 function and coloured by pseudospatial values (left) and the putative lineage (cell-type annotation) (right). **b**, Expression of representative marker genes (*Bmp2*, centre of placode (left); *Sox9*, stem cells (centre); and *Lmo1*, IFE (right)) projected onto pseudospace. **c**, Expression profiles of selected genes in pseudospace. **d**, Heat map of changes in pseudospatial gene expression. Cells were ordered from the placode centre to the IFE region according to pseudospatial values in columns, and genes with non-zero relevance values were classified by *k*-means ($k = 20$) in rows. Selected genes are shown on the right. **e**, Whole-mount RNA in situ hybridization (ISH) of selected genes in **d**. Arrowheads indicate the intended localization of ISH signals. Scale bars, 100 µm. **f**, Concentric gene-expression zone in the placode, summarizing results of whole-mount RNA ISH. Pseudospace scRNA-seq analysis reveals a 2D concentric transcriptional landscape associated with the fates of placode cells.

basal layer of the hair germ stage, whereas H2B–mCherry$^+$ basal cells gave rise to prospective bulge stem cells (Extended Data Fig. 5q, r). Therefore, our findings suggest that the discrepancy in the origin of bulge stem cells is due to the presence of two functionally distinct subpopulations of SOX9$^+$ cells in the placode.

Accurate time-course single-cell RNA sequencing

We examined how epithelial cells changed their cellular states progressively to generate diverse epithelial cells, including prospective bulge stem cells. Embryonic skin tissues contain various types of hair follicle at different developmental stages, which makes the separation and transcriptional profiling of hair follicles at specific developmental stages difficult. We thus developed a ROSA26 reporter line expressing photo-convertible fluorescent protein (nuclear Kikume Green–Red (nKikGR))[15], which enabled us to photo-label target hair follicles under the microscope. Hereafter, all RNA tissue-staining and sequencing data were obtained from embryo skin rather than from explants. Entire single-whisker hair follicles from E12.0, E13.0, E13.5, E14.0, E15.0 and E17.0 embryos were photo-converted (Extended Data Fig. 6a, b, Supplementary Video 9). Photo-converted single cells of the basal epithelium were isolated by fluorescence-activated cell sorting (Extended Data Fig. 6c–l), and then subjected to a sensitive and accurate total single-cell RNA-sequencing (scRNA-seq) technique known as random displacement amplification sequencing (RamDA-seq)[16].

Among sequenced libraries, we identified 962 single-cell transcriptomes of epithelial subpopulations (Extended Data Fig. 7a–c) and assigned them linked embryonic stages in a *t*-distributed stochastic neighbour embedding (*t*-SNE) plot (Extended Data Fig. 7d, e). The transcriptomes appeared to be arranged by stage, and shifted their position gradually from the top left to the bottom right according to embryonic stage. We then identified 16 cell clusters using unbiased clustering (Extended Data Fig. 7f, g). We assigned the in vivo spatial locations of these clusters using in situ hybridization with their cluster marker genes and linked stage information (Extended Data Figs. 7f, h–k, 8). *Lmo1* and *BC100530* (also known as *Cstdc5*) (which mark clusters 5 and 6), *Nfatc1* and *Tgfb2* (which mark clusters 7–12), *Smtn* and *Vdr* (which mark clusters 7, 11 and 13), and *Shh* and *Wnt10b* (which mark clusters 2, 7 and 14) labelled the IFE and infundibulum, upper and lower bulge stem cells, stalk cells and hair germ, respectively. This analysis revealed distinct compartmentalized expression patterns along the longitudinal axis of hair follicles throughout development (Extended Data Fig. 8). When we traced E17.0-derived cell populations from the lower to the upper part of the *t*-SNE plot, the in vivo spatial position of each cell population shifted gradually from the upper to the lower part of the hair follicle (Extended Data Fig. 7k). These data suggest that our scRNA-seq libraries contain a variety of cell types in the epithelia of developing whisker hair follicles with accurate stage and spatial mapping information, which makes these libraries suitable for delineating the spatiotemporal dynamics of cellular-state transitions during hair follicle morphogenesis.

Placode concentric transcriptional zones

To examine whether the 2D concentric lineage zones had already acquired distinct cellular states, we first reconstructed a pseudospace trajectory with E12.0-derived transcriptomes[17,18] (Fig. 3a). Using epithelial lineage markers, we confirmed that cells were 2D-aligned according to their in vivo locations from the placode centre to the IFE (Fig. 3b, c). We used these pseudospace scRNA-seq data to identify 4,342 genes with significant variations of expression across the pseudospace, and sorted them into 20 clusters (Fig. 3d). Many of these genes peaked in the placode centre or IFE regions; however, substantial numbers of genes—including the stem cell markers *Nfatc1* and *Sox9*—showed peaks between these regions. In vivo, the spatially restricted genes showed ring-like expression patterns of different diameters and widths (Fig. 3e, Extended Data Fig. 9a–e), which indicates the presence of concentric zones with gradual gene-expression changes from the placode centre to the IFE (Fig. 3f). This observation is consistent with previous studies that have shown ring-like gene expression around the placode[19,20].

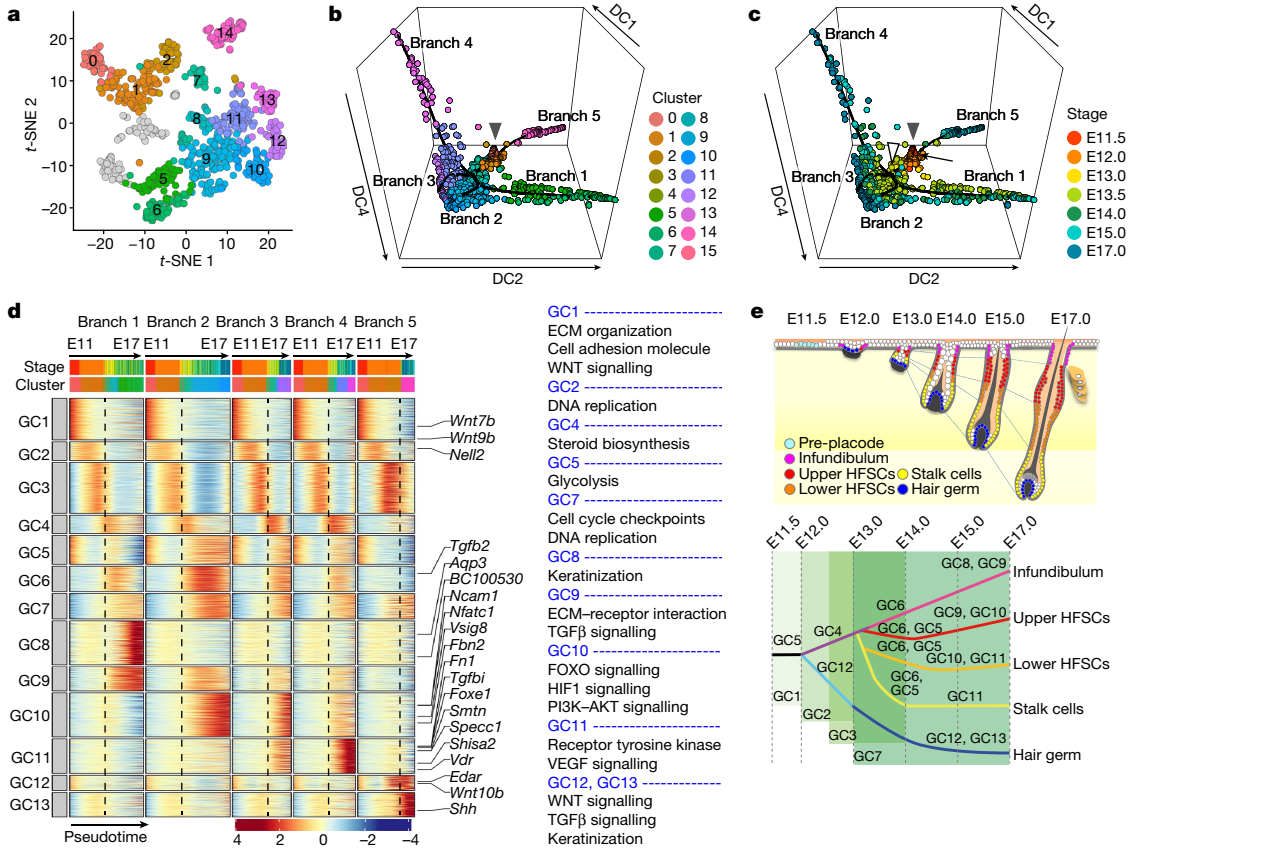

Fig. 4 | Transcriptional landscape that underlies coordinated diversification of epithelial lineages and stem cell induction in the developing hair follicle. a, Epithelial basal cells of the whisker hair follicle are highlighted on the *t*-SNE plot. Cells are coloured according to cell clusters identified in Extended Data Fig. 7f. **b**, **c**, Pseudotemporal ordering of epithelial basal cells of the whisker hair follicle ($n = 862$) on the diffusion map with Slingshot. Black lines represent the estimated trajectories of five lineages. Cells are coloured according to cell clusters (**b**) and embryonic stage (**c**). Closed arrowheads show the root of trajectories (E11.5). Arrow and open arrowhead represent branching points. Branch 1, infundibulum; branch 2, upper stem cells; branch 3, lower stem cells; branch 4, stalk cells; branch 5, hair germ. DC, diffusion component. **d**, Multiway heat map of changes of pseudotemporal gene expression for each of the five branches. The heat map separately describes the gene-expression pattern along each of the developmental branches, as presented at the top of each panel. Cells were ordered by pseudotemporal values in columns, and genes with non-zero relevance values were classified by *k*-means ($k = 13$) in rows. Selected genes and gene ontology (GO) terms are shown on the right. Gene list of gene cluster (GC) 6 raised no valid GO terms (P value < 0.03). ECM, extracellular matrix. **e**, Summary of the transcriptional landscape that underlies epithelial lineage specification during hair follicle development. HFSC, hair follicle stem cell.

We further examined the expression patterns of genes related to particular signalling pathways and found that the basal epithelium of the placode forms gradients of signalling pathway activities from the placode centre to the periphery. The placode periphery is in part characterized by a $WNT^{low}BMP^{high}$ state (the characteristics of adult bulge stem cells[21]) (Extended Data Fig. 9f–j). Consequently, our two marker-independent single-cell omics experiments revealed similar concentric patterns in the basal placode—the lineage concentric zone and the gene-expression concentric zone. Because presumptive bulge stem cells were derived from the border between the placode and the IFE, the outer ring with stem cell marker expression in Fig. 3e, f is highly likely to represent the stem cell origin and its cellular state.

Tissue-wide transcriptional coordination

To analyse how different epithelial populations diversified in developing hair follicles, we reconstructed developmental trajectories of basal epithelial cells with diffusion maps after removing terminally differentiated cells from transcriptomes (Fig. 4a–c, Extended Data Fig. 10a–c). We obtained five-way paths that led to the infundibulum, upper bulge stem cells, lower bulge stem cells, stalk cells and hair germ cells. Even if there was a concentric gene-expression pattern in the E12.0 placode, E11.5- and E12.0-derived cells would tightly cluster at the centre of diffusion maps (owing to the smaller difference in their gene expression compared to mature cells). Despite this, the diffusion map showed that the hair germ lineage first branched at E12.0 (arrows in Fig. 4c, Extended Data Fig. 10a, b), whereas the other lineages diversified from E13.5 (open arrowheads in Fig. 4c, Extended Data Fig. 10a, b). On the basis of information about the reconstructed hair germ lineage and the strong and continuous expression of hair germ lineage markers (*Shh* and *Wnt10b*) in this lineage (Extended Data Figs. 7j, 8, 9a–e), the hair germ lineage developed from hair placode cells through cluster 2 at E12.0, as a part of cluster 7 at E13.0 and then as cluster 14 from E13.5 onward (Extended Data Fig. 10b). Because cells expressing *Shh* and *Wnt10b* appear at E12.0 and remain in the same cluster after E13.5 (Extended Data Figs. 7d, f, 8), we suggest that hair germ cells and their precursors are specified early in the development of hair follicles. On the other hand, we observed strong expression of lineage markers for infundibular cells (*BC100530*), bulge stem cells (*Nfatc1*) and stalk cells (*Vdr*) from E13.0 (Extended Data Fig. 8). From E13.0 to E17.0, these lineages gradually diversified and shifted their location on the *t*-SNE plot (Extended Data Figs. 7d, f, 10b), which suggests that specification and

maturation of non-hair-germ lineages occurred progressively along with hair follicle elongation. The inferred developmental trajectories of upper stem cells (clusters 8, 9 and 10), lower stem cells (clusters 8, 11 and 12) and stalk cells (clusters 11 and 13) were supported by RNA velocity analysis (Extended Data Fig. 10d).

To characterize transcriptional dynamics during hair follicle development, we detected temporally up- and downregulated genes in each lineage progression. We identified 13 gene clusters, which established the ensemble dynamics of gene expression in whole epithelia of developing hair follicles (Fig. 4d, e). Four gene clusters (1, 2, 3 and 7) showed similar changes in gene expression across the five cell lineages, which upregulated at distinct times. Gene cluster 1 was related to interactions between the cell and extracellular matrix, as well as WNT signalling, whereas gene cluster 7 was related to cell proliferation (Fig. 4d, Extended Data Fig. 10e). Conversely, gene clusters 5, 6 and 8–13 represent groups of genes that are coordinately regulated as the infundibulum, upper and lower stem cells, stalk cells and hair germ are induced. Gene clusters 6, 9 and 10 showed genes that are upregulated in late pseudotime of stem cell lineages, and contained many markers and BMP-signalling target genes for adult bulge stem cells (including *Nfatc1*, *Sox9* and *Lhx2*)[22,23] (Extended Data Fig. 10f). Together with the data from the placode stage (Extended Data Fig. 9f–j), our transcriptome analyses suggest that the prospective bulge stem cell lineage acquires a $WNT^{low}BMP^{high}$ state at the placode stage and maintains this cellular state throughout hair follicle development. The induction of upper stem cells was marked by successive waves of gene activation of gene clusters 1–7, 9 and 10, indicating gradual induction through dynamic transcriptional changes (Fig. 4d). Collectively, our single-cell transcriptional analysis identified dynamic waves of 13 transcriptional programmes associated with the diversification of cell lineages (Fig. 4e). These reconstructed cell lineages and their spatial organization were consistent with those that we obtained in direct cell-lineage tracking from live imaging data, which leads us to the conclusion that prospective bulge stem cells are derived from the periphery of 2D concentric zones and develop into the mature, cylindrical stem cell compartments.

Discussion

We built a dynamic atlas of developing hair follicles, which revealed a telescope-like mode of morphogenesis in which each 2D concentric lineage and gene-expression zone in the placode extends to form the longitudinally aligned 3D cylindrical compartments. We propose that this model, which is common to different types of hair follicle, be known as the 'telescope model' for coordinated hair follicle morphogenesis and stem cell induction. Our proposed model resembles the development of the *Drosophila* appendages[4,5], and it might therefore be a general developmental model that underlies the formation of cylindrical structures from the flat placode and the 3D transformation of positional information during ectodermal organ development.

Our findings indicate that the determination of the fate of cells in the placode depends on the position of the cells in the tissue. Several bulge stem cell markers (including *Sox9* and *Nfatc1*) were upregulated at the peripheral zone of the basal layer of the placode in a WNT^{low} BMP^{high} state, which suggests the formation of a primitive niche for the induction of bulge stem cells. Consistent with this notion, a previous study in which *Smad1* and *Smad5* were deleted in the embryonic epidermis resulted in a reduction of the expression of SOX9 and NFATc1 and a lack of prebulge formation[24]. Moreover, small patched activation of β-catenin signalling in the early embryonic epidermis has previously been shown to induce SOX9 expression in the surrounding cells, forming a ring-like zone of SOX9 expression[3]. Thus, WNT or β-catenin signal-active basal epithelial cells at the centre of the placode may induce a $WNT^{low}BMP^{high}$ state in the juxtaposed region. This cellular and extracellular state could serve as a niche for the origin of stem cells, probably under the reaction–diffusion system formed by interplay with the underlying mesenchymal dermal condensate[25,26]. This could be a mechanism to induce the concentric pattern in the placode along with the migration of epithelial and mesenchymal cells towards the centre of the pre-placode[27,28]. Our study provides a foundation for future work to investigate the mechanisms that couple skin organogenesis with signal and cellular compartmentalization, leading to the emergence of stem cells and their niche.

Online content

Any methods, additional references, Nature Research reporting summaries, source data, extended data, supplementary information, acknowledgements, peer review information; details of author contributions and competing interests; and statements of data and code availability are available at https://doi.org/10.1038/s41586-021-03638-5.

1. Xin, T., Greco, V. & Myung, P. Hardwiring stem cell communication through tissue structure. *Cell* **164**, 1212–1225 (2016).
2. Guiu, J. et al. Tracing the origin of adult intestinal stem cells. *Nature* **570**, 107–111 (2019).
3. Ouspenskaia, T., Matos, I., Mertz, A. F., Fiore, V. F. & Fuchs, E. WNT–SHH antagonism specifies and expands stem cells prior to niche formation. *Cell* **164**, 156–169 (2016).
4. Lecuit, T. & Cohen, S. M. Proximal–distal axis formation in the *Drosophila* leg. *Nature* **388**, 139–145 (1997).
5. Ruiz-Losada, M., Blom-Dahl, D., Córdoba, S. & Estella, C. Specification and patterning of *Drosophila* appendages. *J. Dev. Biol.* **6**, E17 (2018).
6. Pispa, J. & Thesleff, I. Mechanisms of ectodermal organogenesis. *Dev. Biol.* **262**, 195–205 (2003).
7. Fujiwara, H., Tsutsui, K. & Morita, R. Multi-tasking epidermal stem cells: beyond epidermal maintenance. *Dev. Growth Differ.* **60**, 531–541 (2018).
8. Solanas, G. & Benitah, S. A. Regenerating the skin: a task for the heterogeneous stem cell pool and surrounding niche. *Nat. Rev. Mol. Cell Biol.* **14**, 737–748 (2013).
9. Nowak, J. A., Polak, L., Pasolli, H. A. & Fuchs, E. Hair follicle stem cells are specified and function in early skin morphogenesis. *Cell Stem Cell* **3**, 33–43 (2008).
10. Liu, Y., Lyle, S., Yang, Z. & Cotsarelis, G. Keratin 15 promoter targets putative epithelial stem cells in the hair follicle bulge. *J. Invest. Dermatol.* **121**, 963–968 (2003).
11. Rhee, H., Polak, L. & Fuchs, E. Lhx2 maintains stem cell character in hair follicles. *Science* **312**, 1946–1949 (2006).
12. Horsley, V., Aliprantis, A. O., Polak, L., Glimcher, L. H. & Fuchs, E. NFATc1 balances quiescence and proliferation of skin stem cells. *Cell* **132**, 299–310 (2008).
13. Xu, Z. et al. Embryonic attenuated Wnt/β-catenin signaling defines niche location and long-term stem cell fate in hair follicle. *eLife* **4**, e10567 (2015).
14. Morita, R. et al. Coordination of cellular dynamics contributes to tooth epithelium deformations. *PLoS ONE* **11**, e0161336 (2016).
15. Tsutsui, H., Karasawa, S., Shimizu, H., Nukina, N. & Miyawaki, A. Semi-rational engineering of a coral fluorescent protein into an efficient highlighter. *EMBO Rep.* **6**, 233–238 (2005).
16. Hayashi, T. et al. Single-cell full-length total RNA sequencing uncovers dynamics of recursive splicing and enhancer RNAs. *Nat. Commun.* **9**, 619 (2018).
17. Qiu, X. et al. Single-cell mRNA quantification and differential analysis with Census. *Nat. Methods* **14**, 309–315 (2017).
18. Qiu, X. et al. Reversed graph embedding resolves complex single-cell trajectories. *Nat. Methods* **14**, 979–982 (2017).
19. Huelsken, J., Vogel, R., Erdmann, B., Cotsarelis, G. & Birchmeier, W. β-Catenin controls hair follicle morphogenesis and stem cell differentiation in the skin. *Cell* **105**, 533–545 (2001).
20. Närhi, K. et al. Sostdc1 defines the size and number of skin appendage placodes. *Dev. Biol.* **364**, 149–161 (2012).
21. Kandyba, E. et al. Competitive balance of intrabulge BMP/Wnt signaling reveals a robust gene network ruling stem cell homeostasis and cyclic activation. *Proc. Natl Acad. Sci. USA* **110**, 1351–1356 (2013).
22. Genander, M. et al. BMP signaling and its pSMAD1/5 target genes differentially regulate hair follicle stem cell lineages. *Cell Stem Cell* **15**, 619–633 (2014).
23. Joost, S. et al. Single-cell transcriptomics reveals that differentiation and spatial signatures shape epidermal and hair follicle heterogeneity. *Cell Syst.* **3**, 221–237 (2016).
24. Kandyba, E., Hazen, V. M., Kobielak, A., Butler, S. J. & Kobielak, K. Smad1 and 5 but not Smad8 establish stem cell quiescence which is critical to transform the premature hair follicle during morphogenesis toward the postnatal state. *Stem Cells* **32**, 534–547 (2014).
25. Saxena, N., Mok, K. W. & Rendl, M. An updated classification of hair follicle morphogenesis. *Exp. Dermatol.* **28**, 332–344 (2019).
26. Maini, P. K., Baker, R. E. & Chuong, C. M. The Turing model comes of molecular age. *Science* **314**, 1397–1398 (2006).
27. Ahtiainen, L. et al. Directional cell migration, but not proliferation, drives hair placode morphogenesis. *Dev. Cell* **28**, 588–602 (2014).
28. Glover, J. D. et al. Hierarchical patterning modes orchestrate hair follicle morphogenesis. *PLoS Biol.* **15**, e2002117 (2017).

Methods

No statistical methods were used to predetermine sample size. The experiments were not randomized, and investigators were not blinded to allocation during experiments and outcome assessment.

Mice

All experimental procedures were approved by the Institutional Animal Care and Use Committee of RIKEN Kobe branch. The care and handling of mice complied with the ethical guidelines of the RIKEN Kobe branch. Mice were housed in a 12h-light/12h-dark cycle and temperatures of 18–23 °C with 40–60% humidity. To visualize epithelial cell nuclei, we generated transgenic mice expressing H2B–eGFP under regulation of the enhancer element of the epithelial keratin *KRT14*[29,30]. H2B–eGFP was subcloned into the BamHI site of the vector containing the *KRT14* promoter. The transgene was injected into zygotes, and then zygotes were transferred into the oviducts of pseudo-pregnant CD1 female mice. Transgenic mice were screened by PCR with forward primer 5′-TGAACCGCATCGAGCTGAAGGG-3′ and reverse primer 5′-TCCAGCAGGACCATGTGATCGC-3′ to detect eGFP. Two lines (*K14-H2B-eGFP* no. 67, accession number CDB0544T-1 and no. 406, accession number CDB0544T-2 (http://www2.clst.riken.jp/arg/TG%20mutant%20mice%20list.html)) were selected from founder mice. Both lines displayed high expression of H2B–eGFP in skin epithelia. However, the line no. 67 expressed H2B–eGFP in the epithelium ubiquitously, and line no. 406 expressed it sparsely. We used line no. 406 for live imaging of whisker hair follicles (HFs) to simplify cell tracking and line no. 67 for live imaging of dorsal HFs to visualize epithelial cells. To isolate cells from the specific types of HFs at specific stages, *R26-CAG-nKikGR* mice (accession number CDB0318K) were generated from conditional *R26R-CAG-nKikGR* mice (accession number CDB0312K) using a previously described strategy[29]. The other mice used in this study are shown in Supplementary Table 4. All mice were bred with albino FVB/NJcl mice (CLEA Japan) or B6(Cg)-Tyrc-2J/J mice (The Jackson Laboratories, JAX stock no. 000058) to avoid imaging interference from melanin deposition.

Histochemical analysis and immunohistochemistry

For fluorescence immunohistochemistry, tissues were embedded in OCT, frozen and cryosectioned (10 μm). The sections were fixed with 4% paraformaldehyde (PFA) in phosphate-buffered saline (PBS) for 5 min at 4 °C. After the blocking, the sections were incubated with the primary antibodies followed by detection using fluorescence-labelled secondary antibodies. All fluorescence microscopy images were captured using Zen (version 2.3) under LSM880 (Carl Zeiss) or LAS X (version 3.5.5) under TCS SP8X (Leica) confocal microscopes.

For whole-mount immunostaining, tissues were fixed with 4% PFA in PBS for 5–60 min at 4 °C. Fixed tissues were washed with PBT (0.1% (v/v) Tween-20 in PBS, pH 7.4) for 30 min three times, stored in PBT at 4 °C, or dehydrated though a series of solutions of methanol in PBT (25%, 50%, 75% and 100% methanol), and then stored at −20 °C. The rehydrated tissues were incubated with the primary antibodies and then incubated with the fluorescence-labelled secondary antibodies. Antibodies used in this study are shown in Supplementary Table 4.

Ex vivo culture of the embryonic whisker pad

Whisker pads were dissected from E11.5–E13.5 mice with needles. The tissue explants were embedded in a drop of collagen type I-A (Nitta gelatin) on a 35-mm lumox-bottomed plastic dish (Sarstedt) or 35-mm glass-bottomed plastic dish (Iwaki) coated with collagen type I-P (Nitta gelatin) and then immersed in Dulbecco's modified Eagle's medium and F-12 nutrient mixture supplemented with 20% fetal bovine serum (GIBCO), 1% penicillin–streptomycin (Sigma), 2 mM GlutaMAX-I supplement (GIBCO), and 100 μg ml^{-1} ascorbic acid (Sigma). The explants were cultured at 37 °C in a humidified atmosphere with 5% CO_2 for up to 7 days. The culture medium was changed at 2-day intervals. Time-course images were captured using AxioVision (version 3.1.2.1) under Axiovert 200M (Carl Zeiss).

Ex vivo culture of the embryonic dorsal skin

Dorsal skin was dissected from E12.5 mice with needles. Skin pieces were embedded in a drop of collagen type I-A (Nitta gelatin) on a 35-mm lumox-bottomed plastic dish (Sarstedt) with the mesenchymal side up. The culture medium was the same as that used for the whisker pad culture. The skin explants were cultured at 37 °C in a humidified atmosphere with 5% CO_2 for up to 11 days. The culture medium was changed at 2-day intervals. Time-course images were captured using AxioVision (version 3.1.2.1) under Axiovert 200M (Carl Zeiss).

Four-dimensional live imaging of embryonic whisker HFs

Live imaging was performed as previously described, with some modifications[14]. In this study, an inverted multiphoton microscope (Olympus, FVMPE-RS or FV1000-MPE) combined with a CO_2 incubator (TOKAI HIT, INUBH-ONICS-F1) was used for the deep imaging of live tissue. Stacks of optical section images (512 × 512 to 800 × 800 pixels for x–y plane and 1 μm for z-axis step, 60–100 slices) were acquired at 10–20-min intervals for 3–5 days using a 25× water-immersion objective lens (Olympus, XLPlanN25XWMP, NA = 1.05, working distance = 2.0 μm) and FV30S-SW (version 1.3.2.86) or FV10-ASW (version 04.02). eGFP was excited at 920 nm using a MAITAI DSHP-OL (Spectra-Physics), and mCherry was excited at 1,100 nm using an InSight DS Dual-OL (Spectra-Physics).

Four-dimensional live imaging of embryonic dorsal HFs

Live imaging of dorsal HFs was done under LSM780 (Carl Zeiss) confocal microscope with Zen software (version 2.3), a CO_2 incubator and a 25× multi-immersion objective lens (Carl Zeiss, LD LCI Plan-Apochromat 25x/0.8 Imm autocorr DIC M27), or under TCS SP8X (Leica) confocal microscope with LAS X software (version 3.5.5), a CO_2 incubator and a 20× multi-immersion objective lens (Leica, HC PL APO 20×/0.75 IMM CORR CS2). Imaging conditions were equivalent to those used for live imaging of whisker HFs with two-photon microscopy. For genetic lineage tracing in live imaging, 4-hydroxytamoxifen (4-OHT) was added to the culture medium (final concentration, 5 μM) to activate Cre recombinase before starting live imaging. After 24 h, the culture medium was replaced with the fresh medium three times to remove 4-OHT by replacement.

Four-dimensional cell tracking analysis

For long-term live imaging of growing HFs, the images were often divided into multiple files to adjust the field of view. To analyse cell behaviour, raw image stacks were processed, concatenated and aligned with ImageJ (version 1.51n), Python (version 3.7.4), Jupyter notebook (version 6.0.1), AutoAligner (version 6.0.1, Bitplane) and Imaris (version 9.2.1 and 8.4.2, Bitplane). The cells were tracked manually using the Imaris Track module with eGFP-labelled H2B expressed under the keratin 14 promoter or mCherry-labelled H2B expressed under the endogenous ROSA26 promoter. Because histones are extremely long-lived, H2B–eGFP is present in the nuclei of keratin-14-positive cells and also retained in their daughter cells including suprabasal cells, enabling observation of epithelial cell division through the development of HFs. Three-dimensional epithelial tissue contours were constructed by 3D rendering using Imaris software based on expression of H2B–eGFP under control of the keratin 14 promoter. In our live imaging data, placodes were identified by condensation of the underlying dermis and following cell cycle arrest detected by the expression of FUCCI probes[27,31,32]. In Fig. 1, forward and retrospective tracking was performed from the hair germ stage. For the analysis in Fig. 2a, b, tracked cells of the placode stage were reassigned into four groups (prospective IFE, and upper, lower and hair germ region) based on Fig. 1d, and we then investigated their cell fate at the hair germ stage.

Cell fates were determined on the basis of the position of the cells in tissue. The threshold for eGFP positivity in Fig. 2d, e was determined on the basis of the intensity of eGFP-negative cells in each time point (Supplementary Table 2).

Analysis of the cell division orientation in live imaging data

Methods to measure the cell division orientation are described step-by-step in Extended Data Fig. 4. In brief, mitotic spindles and basement membrane zones in the developing epithelium were marked in the series of *z*-stack images by the Imaris MeasurementPro module and Imaris Contour Surface, respectively. Three-dimensional *x*–*y*–*z* axis coordinates of daughter cell nuclei and the basement membranes zone were extracted from IMS files, and then the cell division angles against the basement membrane zone were calculated using inverse trigonometric functions. These steps were processed by a custom Python program.

Photo-conversion assay

Embryonic whisker HFs expressing nKikGR (E12.0–E17.0) were dissected, placed on a 35-mm glass-bottomed plastic dish (Iwaki), and visualized with a 488-nm laser under the LSM880 confocal microscope equipped with a 20× Plan-Apochromat objective lens (NA 0.75). Photo-conversion of nKikGR in the area of interest was performed with a 405-nm laser set at 10% power with 1 × 50 iterations. Photo-converted nKikGR was imaged using a 543-nm laser for red fluorescence excitation.

Preparation of single-cell suspensions and fluorescence-activated cell sorting

Photo-converted whisker HFs at each developmental stage (E12.0–E17.0) were dissociated into a single-cell suspension. The dissected tissues were washed in ice-cold PBS and then immersed in a 0.25% trypsin solution (Nacalai) for 5 h at 4 °C. Subsequently, the tissues were treated twice at 37 °C for 5–30 min with 0.25% trypsin and 100 U ml^{-1} DNaseI (Sigma) and then dissociated into single cells by gentle pipetting. The dissociated cells were centrifuged, resuspended in PBS containing 0.5% bovine serum albumin (BSA), and filtered through a 40-μm mesh. The cells were adjusted to 1×10^6 cells per ml and stained with eFluor450-labelled anti-mouse CD31 (1:100, 48-0311-82, eBioscience), PE–Cy7-labelled anti-human/mouse CD49f (ITGA6; 1:100, 25-0495-82, eBioscience), and DAPI (1:2,000). DAPI- and CD31-negative, ITGA6-positive and photo-converted nKikGR-expressing single cells ($DAPI^-CD31^-ITGA6^+KikGR\text{-}red^+$ cells) were directly sorted in 1 μl cell lysis buffer in a 96-well PCR plate (BIOplastics) using a SH800 cell sorter and SH800 software (version 2.1.5, Sony). The cell lysis buffer was prepared as previously described[16]. To isolate epithelial cells immediately before placode formation, the maxillary prominences of E11.5 embryos were dissected, directly treated with trypsin and stained with the above antibodies without photo-labelling ($DAPI^-CD31^-ITGA6^+$ cells) because there is no distinguishable structure leading to hair placode formation. We also collected photo-labelled cells from E13.0 and E15.0 follicles without antibody staining ($DAPI^-KikGR\text{-}red^+$ cells), and we constructed scRNA-seq libraries. Although these libraries contained many mesenchymal-cell-derived libraries, we also used them for the following single-cell transcriptome analysis (Extended Data Fig. 7a–c).

scRNA-seq

scRNA-seq libraries were prepared on the basis of RamDA-seq, a sensitive single-cell full-length total RNA-sequencing method[16]. In particular, we carried out the experiments with reference to the advanced method of RamDA-seq[16]. Fifteen cycles of PCR were applied for library DNA enrichment using a Nextera XT DNA Library Preparation Kit (Illumina). RamDA-seq libraries were quantified and evaluated using a MultiNA DNA-12000 kit (Shimadzu). Subsequently, except for low-quality samples (construction failed or low yield), libraries were pooled at equimolar amounts of 100 fmol. The pooled DNA libraries were sequenced with single-end reads on an Illumina HiSeq 1500/2500 (50 cycles) or NextSeq 500 (75 cycles). The number of input samples was adjusted to obtain 2 million reads per cell. We finally sequenced 1,666 single cell samples.

Analyses of scRNA-seq data

Adaptor trimming and quality assessment of FASTQ files were performed using Fastq-mcf (version 1.04.807) and FastQC (version 0.11.5). The trimmed reads were mapped to the mouse genome (mm10) using HISAT2 (version 2.0.4), and they were categorized as exonic, intronic or intergenic using RseQC (version 2.6.4). Transcript levels were quantified as transcripts per kilobase million (TPM) with Sailfish (version 0.10.0) using the GENCODE v.M14 annotation file. In addition, we used various quality controls to detect poorly performing samples using a combination of Sailfish, RseQC and the featureCounts function of Subread (version 1.5.0). Fifty-two low-quality samples were removed according to the following criteria: the number of mapped reads to a sailfish index (Sailfish) was less than the mean minus three s.d. or the number of assigned reads to gene regions (featureCounts) was less than the mean minus three s.d.; more than 10% of reads were assigned to mitochondrial RNA (featureCounts); showing abnormal gene body coverage of sequencing reads (RseOC). Finally, 1,614 cells (E11.5, 94 cells; E12.0, 276 cells; E13.0, 267 cells; E13.5, 181 cells; E14.0, 177 cells; E15.0, 350 cells; and E17.0, 269 cells) remained for further analysis (Supplementary Table 3).

Further bioinformatics analysis, quantification, statistics and data visualization were mainly performed using R (version 3.4.3) and Python (version 3.7.4) with Jupyter notebook (version 6.0.1). In brief, using the Seurat R package (version 2.3.4 and 3.1.0), we performed data normalization and scaling with the cell cycle regression. We then performed *t*-SNE clustering with the first 20 principal components, identified clusters using the FindClusters function on the basis of a shared nearest neighbour modularity optimization-based clustering algorithm, and detected highly variable genes in each cluster using the FindAllMarkers function[33]. Cell types in each cluster were determined using a combination of marker genes identified from literature, GO detected by a web-based tool (Enrichr) and gene-expression profiles obtained by ISH. No significant plate-to-plate variations (batch effects between plates) were confirmed by visualizing the distribution of each plate-derived library on the dimensional reduction plot without correction of batch effects (Extended Data Fig. 7e).

RNA velocities in single cells were calculated with a Python program, velocyto version 0.17.15 (http://velocyto.org)[34], and the vectors that predicted the future state of individual cells were overlaid on the *t*-SNE plot obtained by Seurat.

The pseudospace in Fig. 3a was reconstructed by applying a semi-supervised approach implemented in Monocle2 (version 2.6.4)[17,18] using E12.0 epithelial libraries derived from three plates: the two plates used in Extended Data Fig. 7d plus one plate for which library preparation was performed after storage at −80 °C for 2 years. Because one added plate showed some batch effect, the residualModelFormulaStr function in Monocle2 was used to regress out the batch effect and cell cycle effect. We defined *Shh* and *Bmp2* as markers for the centre of placode, *Lmo1* and *Wnt4* as IFE markers, and *Nfatc1* as a stem cell (SC) marker on the basis of our whole-mount ISH results. Then, we selected the top 1,000 genes that covaried with the lineage markers and used them to order cells in pseudospace. DDRTree was used for dimensionality reduction, and the reconstructed trajectory was plotted in two dimensions. The differentially expressed genes in pseudospace were detected by Monocle functions. Genes related to signalling pathways in pseudospace of the hair placode were selected from the differentially expressed genes in pseudospace on the basis of the gene lists of the KEGG PATHWAY database.

To reconstruct the developmental trajectory of epithelial basal cells derived from E11.5–17.0 whisker HFs in Fig. 4, we first removed

non-basal epithelial cells, such as keratinized cells and Merkel cells. Then, we reanalysed the remaining datasets with destiny package (version 2.12.0) for Diffusion map[35], and we detected cell trajectories using the Slingshot package (version 1.0.0)[36] with cluster information determined by Seurat. The pseudotime was constructed by setting E11.5-derived cells as the root. We manually split the CellDataSet into five distinct CellDataSets, each of which contained the common progenitor cells and one of the five differentiated lineage branches. Then, we detected temporally expressed genes through each lineage branch using Monocle BEAM functions. Heat maps and expression plots were generated using the ComplexHeatmap (version 2.2.0) and ggplot2 package (version 3.1.0). Gene set enrichment analysis was carried out in the clusterProfiler package (version 3.14.3)[37]. A custom R script was used to output the figures.

Probe synthesis for ISH

Templates for probe synthesis were produced by PCR using cDNA derived from E12.0 and E17.0 mouse embryos. The sequences of each primer pair are shown in Supplementary Table 4. RNA probes were synthesized and labelled with DIG RNA Labelling Mix and T7 RNA Polymerase (Roche).

ISH

ISH was performed using 10-μm-thick frozen sections as previously described[38]. Stained sections were washed with PBS, stored in Ultramount Permanent Mounting Medium (DAKO), and photographed using cellSens (version 1.18) under an Olympus BX53 microscope with a DP73 camera.

Whole-mount ISH

Mouse embryos were fixed overnight at 4 °C in fresh 4% PFA, dehydrated though a series of solutions of methanol in PBT (25%, 50%, 75% and 100% methanol), and then stored at −20 °C. The dehydrated fixed embryos were rehydrated, rinsed twice in PBT, and then digested with proteinase K (10 μg ml^{-1} in PBT) for 25 min at room temperature. After washing once with 2 mg ml^{-1} glycine in PBT and twice with PBT, the embryos were post-fixed in 4% PFA and 0.2% glutaraldehyde in PBT for 20 min at room temperature. All embryos were bleached with 6% hydrogen peroxide in PBT for 1 h, washed 3 times with PBT and transferred to the hybridization solution (50% formamide, 10 mM Tris-HCl (pH 7.5), 5% (w/v) dextran sulfate, 1× Denhardt's solution, 600 mM NaCl, 0.25% (w/v) SDS, 1 mM EDTA and 200 μg ml^{-1} *Escherichia coli* tRNA). One-hour prehybridization and overnight hybridization were carried out at 65 °C. Then, the embryos were washed with a solution (50% formamide, 1× SSC (pH 4.5) and 0.1% (v/v) Tween-20) at 65 °C for 1 h. After washing with MABT (300 mM NaCl, 100 mM maleic acid and 0.1% (v/v) Tween-20) and blocking, the hybridized probe was detected using an alkaline phosphatase-conjugated anti-digoxigenin antibody (Roche). Colour development was carried out with BCIP and NBT substrate solution. Stained embryos were washed with PBT, stored in a solution of glycerol in PBT, and photographed using LAS (version 4.13) under a Leica MZ165FC stereomicroscope.

Whole-mount RNAscope ISH

Mouse embryos were collected and stored at −20 °C as described in 'Whole-mount ISH'. After rehydrating the embryos and washing them in PBT, dorsal skin samples were dissected from them. The samples were treated with RNAscope hydrogen peroxide (Advanced Cell Diagnostics) for 1 h at room temperature, washed 3 times with PBT then incubated in the target probe mixture at 40 °C overnight. RNA detection was performed according to RNAscope Multiplex Fluorescent Reagent Kit v.2 using tyramide dye fluorophores (The Opal 4-Colour Manual IHC Kit, AKOYA biosciences) diluted in RNAscope TSA dilution buffer. All incubations were performed at 40 °C, and after each reaction step, the samples were washed 3 times with the RNAscope wash buffer for 5 min. The samples were then stained with DAPI solution overnight at 4 °C with slow agitation. Before imaging, samples were rinsed in PBT, mounted in ProLong Gold Antifade Mountant (Thermofisher). The probes used are shown in Supplementary Table 4.

Figure preparation

Images in figures were processed using IMARIS (version 9.2.1 and 8.4.2, Bitplane), ImageJ (version 1.51n) and assembled into the panel using Adobe Photoshop (version 21.2.6) and Adobe Illustrator (version 25.2.1).

Study design

The experiments were not randomized. Experimental groups were determined by genotype of mice. Both male and female embryos were used in experiments. In most of the experiments, no blinding method was possible as only one experimenter was performing the analysis.

Statistical analysis and reproducibility

No statistical method was used to predetermine sample size. In this study, we analysed a total of 14 HFs; two whisker HFs for the analysis from the placode stage to hair germ stage, two whisker HFs for the analysis from the hair germ stage to bulbous peg stage, one whisker HF for the analysis from the placode stage to bulbous peg stage and nine dorsal HFs for the analysis from the placode stage to hair germ stage. These samples were derived from several different reporter mouse lines. Although each quantitative analysis of cell tracking was performed on three or four HFs (sometimes from different reporter mouse lines), each replicate (HF) derived data contained a large amount of cell lineage information that showed a low variation between HFs and low *P* values. They provided essentially the same multicellular dynamics regardless of HF type or reporter mouse line (Figs. 1, 2, Extended Data Figs. 3, 5 and their Source Data). This indicated high data reproducibility between HFs both for whisker and dorsal HFs. The detailed sample size information, including analysed cell lineage numbers, is summarized at Supplementary Tables 1, 2. The detail of biological replicates in each panel is summarized as below.

In Fig. 1b and Extended Data Fig. 3e, f, the cell tracking experiments were performed with the data from three independent experiments, one HF each, and each tracking experiment showed similar results. In Fig. 1d, e and Extended Data Fig. 3h, i, the cell tracking experiments were performed with the data from three independent experiments, one HF each, and each tracking experiment showed similar results. In Fig. 2a, b and Extended Data Fig. 5a, b, the cell tracking experiments were performed with the data from three independent experiments, one HF each, and each tracking experiment showed similar results. In Fig. 2d, e, f, Extended Data Fig. 5m–o, the cell tracking experiments were performed with the data from three independent experiments, one HF each, and each tracking experiment showed similar results. In Extended Data Fig. 5j–l, the cell tracking experiments were performed with the data from three independent experiments, one HF each, and each tracking experiment showed similar results. In Extended Data Fig. 5q, r, the cell tracking experiments were performed with the data from three independent experiments, one or two HF each, and each tracking experiment showed similar results.

The following statistical analyses were used to determine the significance in experiments. In Extended Data Figs. 3f, 5a, b, one-way analysis of variance (ANOVA) followed by Tukey's test; in Fig. 1d and Extended Data Fig. 5j, two-sided nested *t*-test; in Figs. 1e, 2d,e and Extended Data Fig. 5k, q, two-sided Fisher's exact test; and in Extended Data Fig. 3h, two-sided unpaired *t*-test. Statistical analyses were performed using GraphPad Prism (version 9.0.2), and R (version 3.4.3). Statistically significant differences are indicated in each figure ($^{*}P < 0.05$, $^{**}P < 0.01$, $^{***}P < 0.001$ and $^{****}P < 0.0001$). Graphs were generated by GraphPad Prism and R. We show representative micrographs that came from at least two biological replicates.

Reporting summary

Further information on research design is available in the Nature Research Reporting Summary linked to this paper.

Data availability

Live imaging data in this study have been deposited in the SSBD repository at https://doi.org/10.24631/ssbd.repos.2020.06.002 and http://ssbd.qbic.riken.jp/set/20200602/. The scRNA-seq data in this study have been deposited in the Gene Expression Omnibus under accession code GSE147372. The mouse genome (mm10) used in this study is available at https://genome.ucsc.edu/. The web-based tool Enrichr is available at https://maayanlab.cloud/Enrichr/. The KEGG PATHWAY database is available at https://www.genome.jp/kegg/. Any other relevant data are available from the corresponding author upon reasonable request. Source data are provided with this paper.

Code availability

Scripts used for scRNA-seq analysis are available at https://github.com/FujiwaraLab/Morita_et_al_2021 and source code for analysis of the cell division orientation in live imaging data is available at https://github.com/RIKEN-PHB/Morita-Paper-Spindle-Analysis.

29. Abe, T. et al. Establishment of conditional reporter mouse lines at ROSA26 locus for live cell imaging. *Genesis* **49**, 579–590 (2011).
30. Vassar, R., Rosenberg, M., Ross, S., Tyner, A. & Fuchs, E. Tissue-specific and differentiation-specific expression of a human K14 keratin gene in transgenic mice. *Proc. Natl Acad. Sci. USA* **86**, 1563–1567 (1989).
31. Sakaue-Sawano, A. et al. Visualizing spatiotemporal dynamics of multicellular cell-cycle progression. *Cell* **132**, 487–498 (2008).
32. Biggs, L. C. et al. Hair follicle dermal condensation forms via Fgf20 primed cell cycle exit, cell motility, and aggregation. *eLife* **7**, e36468 (2018).
33. Stuart, T. et al. Comprehensive integration of single-cell data. *Cell* **177**, 1888–1902 (2019).
34. La Manno, G. et al. RNA velocity of single cells. *Nature* **560**, 494–498 (2018).
35. Angerer, P. et al. destiny: diffusion maps for large-scale single-cell data in R. *Bioinformatics* **32**, 1241–1243 (2016).
36. Street, K. et al. Slingshot: cell lineage and pseudotime inference for single-cell transcriptomics. *BMC Genomics* **19**, 477 (2018).
37. Yu, G., Wang, L. G., Han, Y. & He, Q. Y. clusterProfiler: an R package for comparing biological themes among gene clusters. *OMICS* **16**, 284–287 (2012).
38. Nakao, K. et al. The development of a bioengineered organ germ method. *Nat. Methods* **4**, 227–230 (2007).

Acknowledgements We thank S. Kuraku and O. Nishimura for assistance with RNA sequencing and data processing; the RIKEN Genome Network Analysis Support Facility (GeNAS) for RNA sequencing; RIKEN Kobe Light Microscopy Facility, Laboratory for Animal Resources and Genetic Engineering and Unit for Four-Dimensional Tissue Analysis for technical assistance; F. Matsuzaki for critical reading of the manuscript; T. Matsuzaki for an important suggestion related to the telescope model; S. Onami for discussions; M. Morimoto for providing a mouse line; A. Iijima for help with cell tracking analysis; and A. Matsushima and M. Ishii for their assistance with the infrastructure for the data analysis. This work was supported by a RIKEN intramural grant, the RIKEN Single Cell Project, the Platform Project for Supporting in Drug Discovery and Life Science Research from MEXT and AMED and the JST CREST program (JPMJCR1926) to H.F. and JSPS Grant-in-Aid for Young Scientists (B) (15K19709 and 17K16361), JSPS Grant-in-Aid for Scientific Research (C) (19K08763), the RIKEN BDR-Otsuka Pharmaceutical Collaboration Center (RBOC) founding program and a Shiseido Female Researcher Science Grant to R.M. This work was partially supported by JST CREST grant number JPMJCR16G3 to I.N.

Author contributions R.M. and H.F. conceived the project, designed experiments and wrote the manuscript. R.M. performed most of the experiments and bioinformatics and analysed the data. N.S. and H.S. assisted with cell tracking analysis and histological analysis. T.H. and M.U. performed the library preparation for the RamDA-seq. M.Y. and R.M. performed the bioinformatics analyses. I.N. supervised scRNA-seq experiments and bioinformatics analyses. T.Y. and T.S. provided the custom Python program to analyse the orientation of cell division. T.A., H.K. and Y.F. generated *R26-CAG-nKikGR*, *R26R-CAG-nKikGR* and *K14-H2B-eGFP* mice, and assisted with mouse experiments. H.F. supervised the project.

Competing interests The authors declare no competing interests.

Additional information

Supplementary information The online version contains supplementary material available at https://doi.org/10.1038/s41586-021-03638-5.

Correspondence and requests for materials should be addressed to H.F.

Peer review information *Nature* thanks Maria Kasper, Michael Rendl and the other, anonymous, reviewer(s) for their contribution to the peer review of this work. Peer reviewer reports are available.

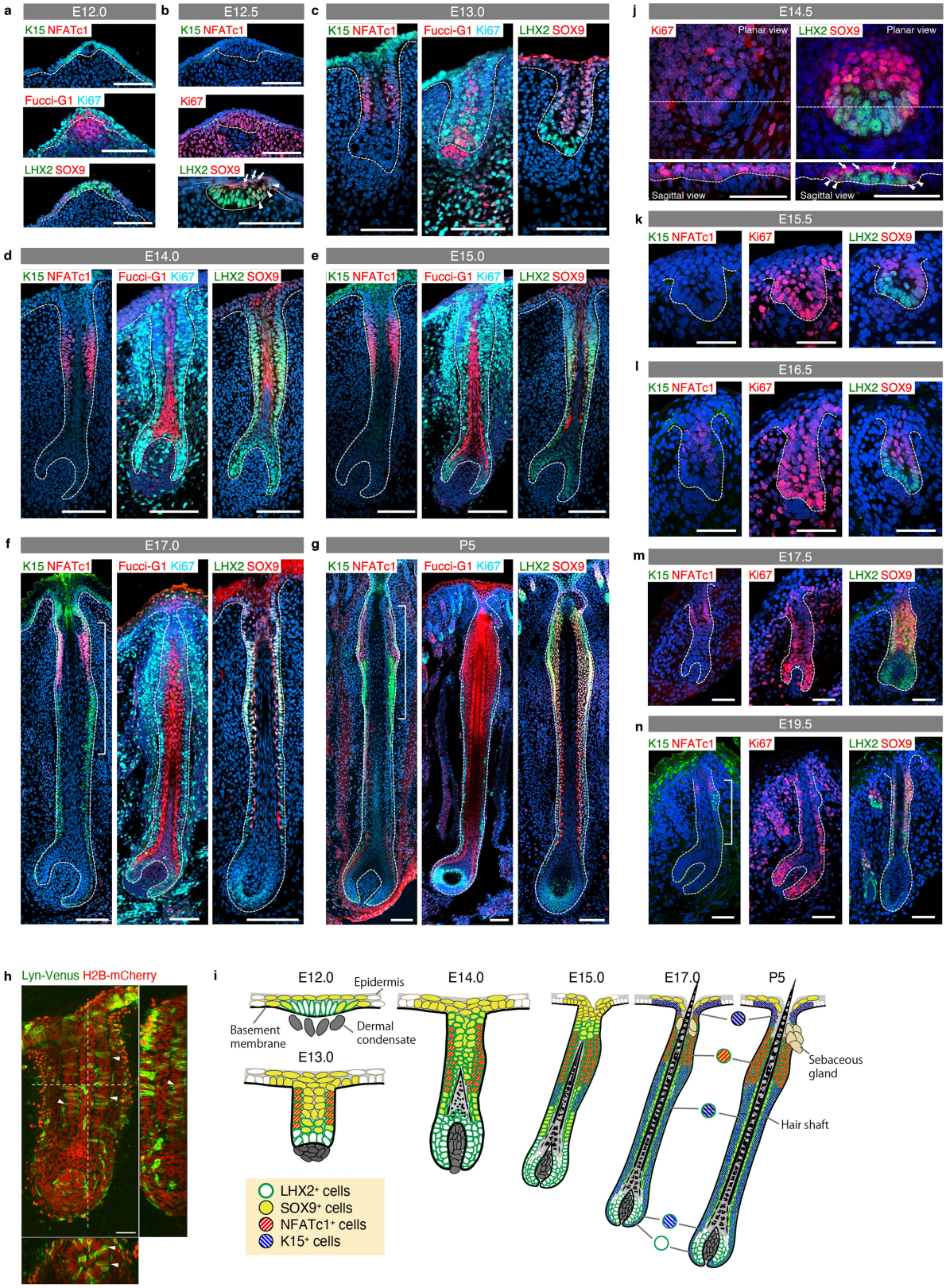

Extended Data Fig. 1 | See next page for caption.

Extended Data Fig. 1 | Origin and early lineage of bulge stem cells cannot be traced by expression of known adult stem cell markers. **a**–**g**, Immunohistochemistry of developing whisker hair follicles (HFs) for known stem cell (SC) markers at E12.0 (**a**, early hair placode), E12.5 (**b**, late hair placode), E13.0 (**c**, hair germ), E14.0 (**d**), E15.0 (**e**), E17.0 (**f**) and post-natal day (P)5 (**g**). LHX2 was expressed in the basal cells of the placode, while K15 and SOX9 were detected in suprabasal and peripheral basal cells of the placode (**a**). At the late placode stage (E12.5), SOX9 was strongly expressed in the flat suprabasal cells of the placode (arrows in **b**) and also in some basal cells located near the placode periphery (arrowheads in **b**). NFATc1 was undetectable throughout these stages (**a**, **b**). Thus, at the onset of HF morphogenesis, the expression patterns of adult SC markers vary and there is no clear region in which all SC markers overlap. From the hair germ stage (E13.0) onward, NFATc1 appeared in whisker HFs, and its expression was always restricted to the upper region of the HF (**c**–**g**). NFATc1-positive epithelial cells formed a compartment with pseudo-stratified (see **h**) and bulge-like morphology (**d**–**g**) with gradual loss of the expression of mitotic marker Ki67 during follicle development (**a**–**g**), which are typical characteristics of adult bulge HFSCs. SOX9 and LHX2 expression also became restricted to the middle to upper part of the HF after E14.0 (**d**–**g**). The expression patterns of SC markers in E17.0 follicles were almost equivalent to those seen in the upper half of P5 mature follicles, in which a large bulge-like epithelial structure was evident (brackets in **f**, **g**). Taken together, these results indicate that basal epithelial cells acquire compartmentalized SC marker expression patterns of the mature bulge by E17.0 in whisker HFs. The origin and early lineage of bulge SCs cannot be traced by following the expression of known adult SC markers because of their wide variation in expression patterns of the hair placode, hair germ and bulbous peg stages. Thus, at present, there is no marker that can exclusively label the origin and early lineage of prospective SCs from the placode stage. Scale bars, 100 μm. **h**, Three-dimensional-reconstructed *z*-stack images from whisker HFs derived from *KRT5-cre;R26R-Lyn-Venus;R26-H2B-mCherry* at E14.0. Cell membranes were sparsely labelled by Venus. Arrowheads indicate the pseudo-stratified epithelium. Scale bar, 50 μm. **i**, Summary of known SC marker expressions in the developing whisker HF. **j**–**n**, Immunohistochemistry of developing dorsal HFs for known SC markers at E14.5 (**j**, hair placode), E15.5 (**k**, hair germ), E16.5 (**l**), E17.5 (**m**) and E19.5 (**n**). SOX9-positive cells were localized in the suprabasal layer (arrows in **j**) and in the basal layer near the placode periphery (arrowheads in **j**) in the dorsal HF placode as observed in the whisker HF placode. Morphogenetic events and marker expression patterns closely resemble those of whisker HFs. Scale bars, 50 μm.

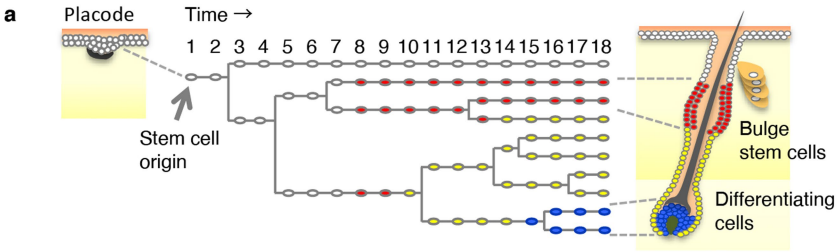

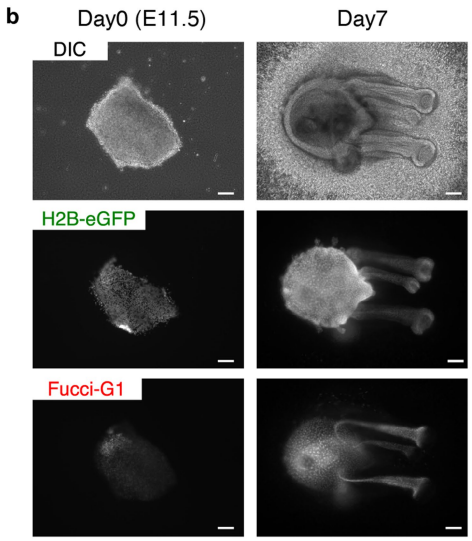

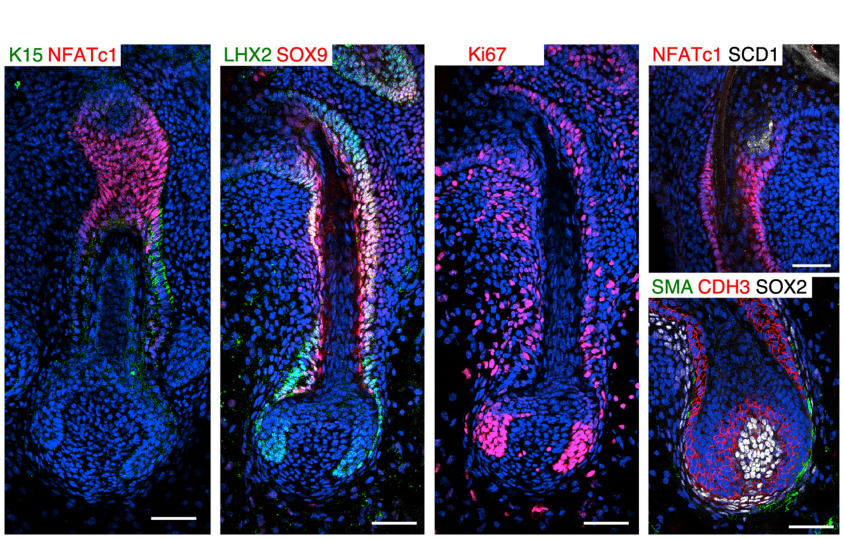

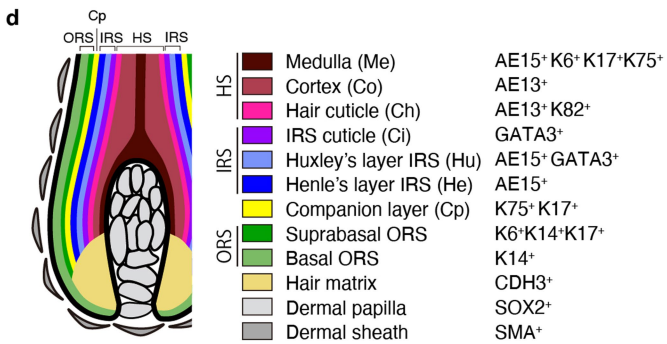

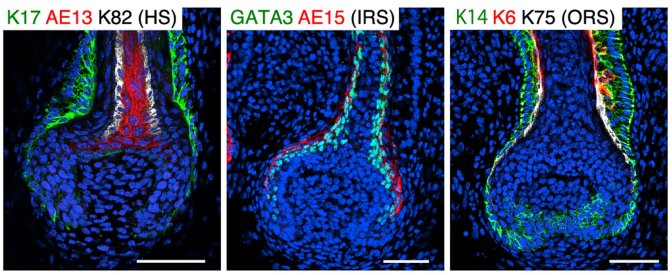

Extended Data Fig. 2 | Ex vivo culture system of developing whisker HFs. **a**, Strategy to identify the origin and lineage dynamics of HF epithelial cells. **b**, Photographs of ex vivo cultured whisker pad derived from E11.5 *K14-rtTA ;TetO-H2B-eGFP;Fucci-G1* mice on day 0 and day 7. Scale bars, 100 µm. **c**, Immunostaining of whisker HFs derived from E11.5 embryos on day 6 of ex vivo culture. Antibodies detected upper (NFATc1$^+$SOX9$^+$LHX2$^+$) and lower (KRT15$^+$SOX9$^+$LHX2$^+$) stem cell compartments, proliferative cells (Ki67$^+$), sebaceous glands (SCD1$^+$), hair matrix (CDH3$^+$), dermal sheaths (SMA$^+$) and dermal papilla cells (SOX2$^+$). Scale bars, 50 µm. **d**, Immunostaining of day-6 ex vivo cultured whisker HFs derived from E11.5 embryos for hair cell layer markers shown in the left panel. Ex vivo developing whisker HFs had unique cellular layers characteristic of HFs, except for the medulla, which is formed in mature HFs. HS, hair shaft; IRS, inner root sheath; ORS, outer root sheath. Scale bars, 50 µm.

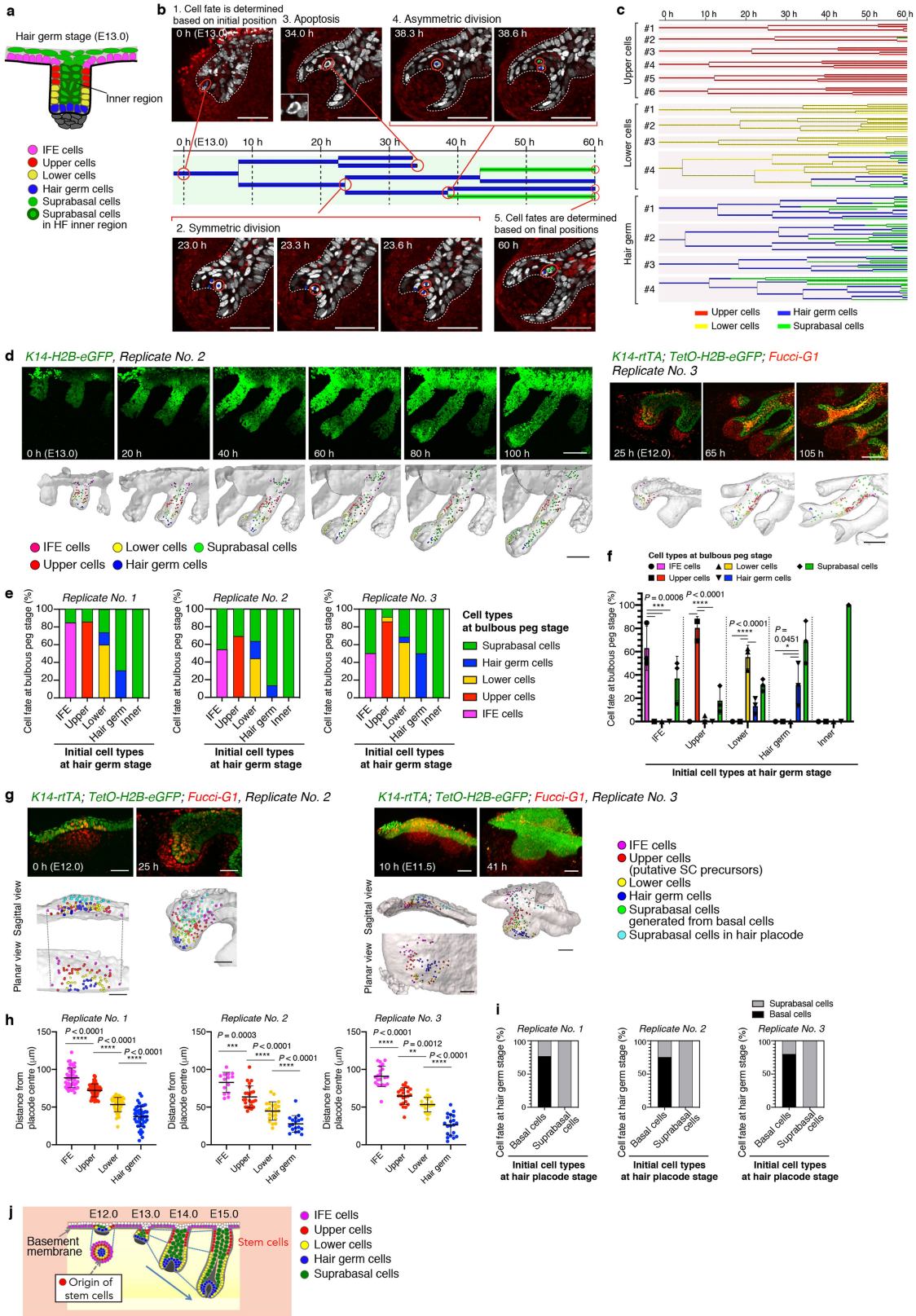

Extended Data Fig. 3 | See next page for caption.

Extended Data Fig. 3 | Identification of the origin and lineage dynamics of HF epithelial cells by long-term live imaging. a, Schema of epithelial cell subpopulations at the hair germ stage, which we defined for cell tracking. Magenta, IFE basal cells; red, basal cells located in the upper half of the HF; yellow, basal cells located in the lower half of the HF; blue, cells adjacent to the dermal papilla; green, suprabasal cells in the IFE or HF. **b**, Lineage tree reconstructed from tracking of a hair germ cell and its progeny. The *x* axis shows the duration of imaging. Lineage is colour-coded based on cell fate, and cell fate was identified based on the cell position in tissue. Scale bars, 50 μm. **c**, Examples of lineage trees of tracked upper, lower and hair germ cells in Fig. 1a. **d**, **e**, HF development is accomplished by enlarging each earlier compartment longitudinally aligned in the follicle epithelium. Data of replicate whisker HFs related to Fig. 1a, b are shown. **d**, Snapshot images (top panels) and lineage tracking data (bottom panels) of long-term continuous imaging of whisker HF development from the hair germ to bulbous peg stage. Different epithelial lineages were longitudinally aligned as 3D cylindrical compartments in HFs, and prospective bulge SCs were located in the upper part of the HF as shown in Fig. 1a (replicate no. 1, represented in the main figure). Scale bars, 100 μm. **e**, Cell fates of epithelial cells in the IFE, upper, lower, hair germ and inner regions of the hair germ stage. Cell fates at the bulbous peg stage are shown. **f**, Bar plot converted from stacked bar plot of Fig. 1b. Statistical analysis was performed by one-way ANOVA followed by Tukey's test. **g**–**i**, Different epithelial lineages are aligned in a concentric manner in the placode. Replicate whisker HFs related to Fig. 1c–e are shown in **g**–**i**. **g**, Snapshot images (top panels) and lineage tracking data (bottom panels) of long-term continuous imaging of whisker HF development from the placode stage to hair germ stage. Origin of prospective bulge SCs (red) was located at the periphery of the hair placode as shown in Fig. 1c (replicate no. 1, represented in the main figure). Scale bars, 50 μm. **h**, Bee swarm plot showing the distances of cells from the placode centre. Different epithelial lineages were aligned in a concentric manner in the placode. Statistical analysis was performed by two-sided unpaired *t*-test. **i**, Fate of basal and suprabasal cells of the hair placode stage. Cell fates at the hair germ stage are shown. **j**, Summary of the developmental origins and lineage dynamics of HF epithelial cells. The embryonic stage at which imaging started is indicated in each figure. Each value in the graph is the mean ± s.d. from three independent experiments, one HF each. Numbers of analysed cell lineages are summarized in Supplementary Table 1. See also 'Statistical analysis and reproducibility' in Methods and Source Data.

a Marking mitotic spindles in the developing epithelium.

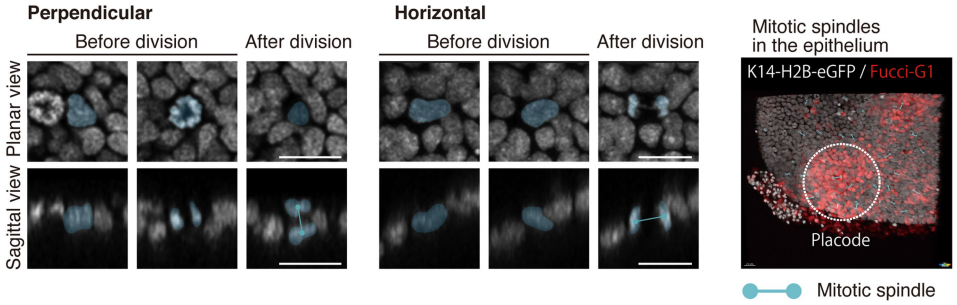

b Extraction of positional information of the basement membrane zone.

1) Surface rendering of the developing epithelium based on the intensity of K14 promoter-driven eGFP.

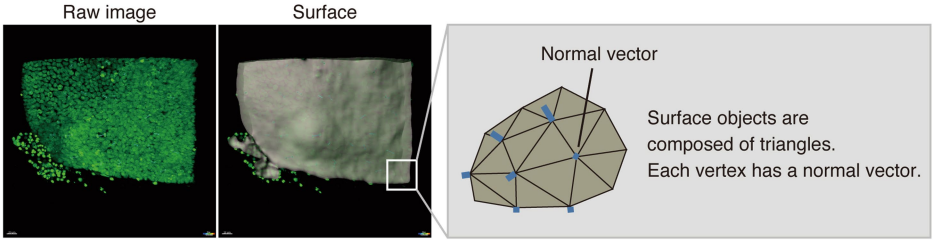

2) Extraction of the dermis-side surface as the basement membrane zone based on the direction of the normal vectors.

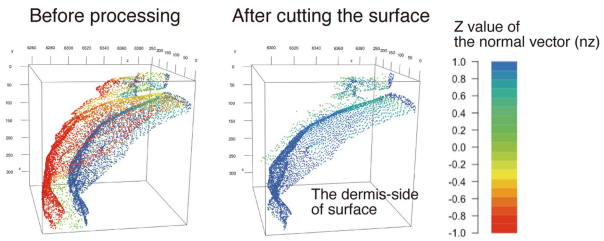

c Calculation of spindle orientation angle relative to the basement membrane zone.

1) Finding the closest vertex and its associated normal vector on the dermis-side surface by calculating the distance between the centre of a mitotic spindle and each vertex.

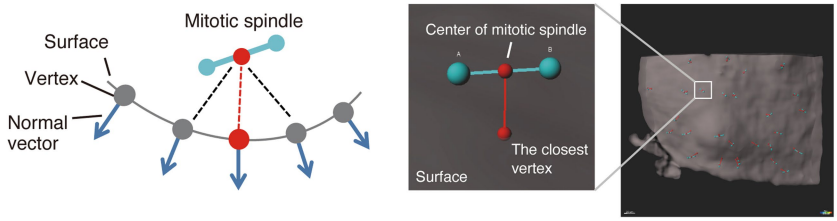

2) Calculation of spindle orientation angle relative to the normal vector.

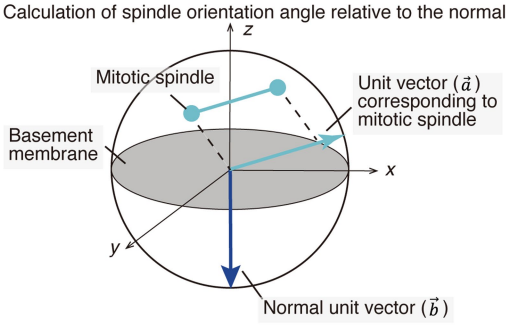

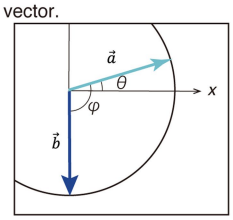

$\vec{a} \cdot \vec{b} = \cos\varphi$

$\varphi = \cos^{-1}(\vec{a} \cdot \vec{b})$

$\theta = \left|\frac{\pi}{2} - \varphi\right|$ ≈ the spindle orientation angle relative to the basement membrane zone

Extended Data Fig. 4 | See next page for caption.

Extended Data Fig. 4 | Measurement of cell division angles in the developing epithelium. In 3D live imaging data, morphology of the developing epithelium was changing constantly. Accordingly, the basement membrane zone was also bending, but not flat. Therefore, we calculated the cell division orientation relative to the basement membrane zone in the developing epithelium three-dimensionally as shown here. **a**, We first marked the dividing cells in the placode and surrounding IFE in live imaging data, based on chromosome condensation. Examples of a perpendicular (left panels) and horizontal division (middle panels) relative to the basement membrane zone, which were pseudo-coloured in blue; the mitotic spindle axis is indicated by a cyan line connecting the daughter-cell nuclei. The top panels are a planar view images of the epithelium, and the bottom panels are sagittal view images of the epithelium. The placode region in the epithelium was distinguished by accumulation of Fucci-G1 signals accompanied by condensation and cell cycle arrest of the underlying dermal cells, as shown by the dashed circle in the right panel. Scale bars, 20 μm. **b**, To extract positional information of the basement membrane zone, we next obtained the surface of the developing epithelium based on expression of *K14-H2B-eGFP* using the surface rendering function in Imaris. A surface object in Imaris was constructed as a mesh object consisting of triangles and vertex normal vectors. Then, based on the direction of the normal vectors, we cut the surface of the opposite side of the basement membrane zone (outer surface of the epithelium) and substituted the remaining dermis-side surface for the basement membrane zone. **c**, We calculated the 3D orientation of cell division to the basement membrane zone using x–y–z axis coordinates of the mitotic spindle axis and basement membrane zone. In brief, we first found the closest vertex and its associated normal unit vector on the dermis-side surface by calculating the distance between the centre of a mitotic spindle and each vertex. The cell division angle to the basement membrane zone was then calculated from an inner product of the closest vertex normal unit vector and the unit vector corresponding to a mitotic spindle.

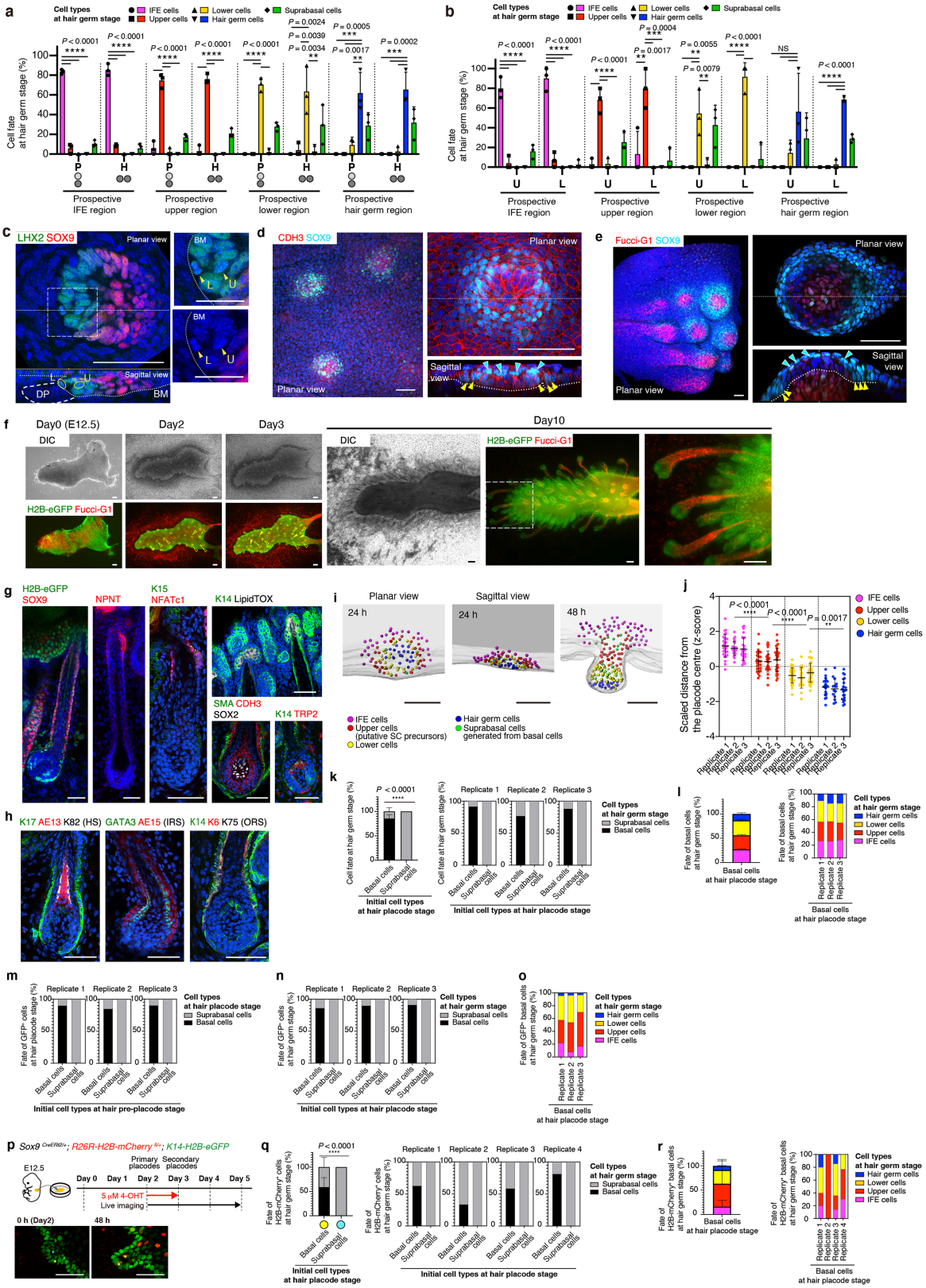

Extended Data Fig. 5 | See next page for caption.

Extended Data Fig. 5 | Placode cell fate is determined by cell position but not cell division orientation. a, **b**, Bar plots were converted from the stacked bar plot in Fig. 2a, b, respectively. Statistical analysis was performed by one-way ANOVA followed by Tukey's test. **c**, Upper and lower daughter cells after perpendicular division in late placode basal layer are marked by LHX2, while the SOX9$^+$ suprabasal nuclei are not labelled with LHX2. This suggests that upper daughter cells hold transcriptional similarity to the basal layer and remain in the pseudo-stratified basal layer. E14.5 dorsal HFs in embryonic skin tissue (not explants) were immunostained for SOX9 and LHX2. Cell division was identified by chromosome condensation. Dashed box shows magnified region (right panels). BM, basement membrane; DP, dermal papilla; U, upper daughter cell; L, lower daughter cell. Scale bars, 50 μm. **d**, **e**, Localization of SOX9$^+$ cells in HF placodes in vivo. E14.5 dorsal HFs (**d**) and E12.0 whisker HFs (**e**) in embryonic skin tissues (not explants) were immunostained for SOX9 and CDH3. Hair placodes were detected with CDH3 expression or Fucci-G1 probe fluorescence signals. SOX9 expressions were detected not only in flat suprabasal cells (cyan arrowheads) but also in basal cells (yellow arrowheads) located at the periphery of the hair placode. Scale bars, 50 μm. **f**, Photographs of ex vivo cultured dorsal skin of E12.5 *K14-rtTA;TetO-H2B-eGFP;Fucci-G1* mice on days 0, 2, 3 and 10. Yellow open arrowheads and filled arrowheads indicate first-wave and second-wave hair placodes, respectively. Dashed box shows magnified region (right). Scale bars, 100 μm. **g**, Immunostaining of dorsal HFs in day-9 ex vivo culture of E12.5 dorsal skin. The following tissue compartments were detected: bulge stem cells (NFATc1$^+$SOX9$^+$NPNT$^+$KRT15$^+$), sebaceous glands (LipidTOX$^+$), hair matrix (CDH3$^+$), dermal sheaths (SMA$^+$), dermal papilla cells (SOX2$^+$) and melanocyte (TRP2$^+$). Scale bars, 50 μm. **h**, Immunostaining of day-9 ex vivo cultured dorsal HFs derived from E12.5 embryos for hair cell layer markers shown in Extended Data Fig. 2d. Ex vivo developing dorsal HFs had distinct cellular layers characteristic of HFs except for the medulla, which is formed in mature HFs. Scale bars, 50 μm. **i**, Lineage tracking data of long-term continuous imaging of dorsal HF development from the placode stage to the hair germ stage, which correspond to the bottom panels in Fig. 2c. Origin of prospective bulge SCs (red) was located at the periphery of the hair placode as observed in the whisker HF placode. Scale bars, 50 μm. **j**, Bee swarm plot of the distances of dorsal hair placode cells from the placode centre. HFs used for measurement were from cultured dorsal HFs of *K14-rtTA;TetO-H2B-eGFP;Fucci-G1* and *Sox9$^{IRES\text{-}eGFP/+}$;R26-H2B-mCherry* mice. Values were scaled based on the diameter of each placode. Different epithelial lineages were aligned in a concentric manner in the placode. Two-sided nested *t*-test was used. **k**, Fate of basal and suprabasal cells in the dorsal HF placode analysed in **i**. Cell fates at the hair germ stage are shown. Summarized data are shown in the left panel, and the data for corresponding replicate HFs are shown in the right panels. Two-sided Fisher's exact test was used. **l**, Stacked bar plots showing the lineage distribution of placode basal cells in the dorsal HF at the hair germ stage. Cells grouped in the black bar in **k** were examined. Summarized data are shown in the left panel, and the data for corresponding replicate HFs are shown in the right panel. **m**–**o**, Replicate HFs related to Fig. 2d–f are shown in **m**–**o**. **m**, Fate of basal and suprabasal cells in pre-placodes of *Sox9-IRES-eGFP* reporter derived dorsal skin explants. Fate of GFP$^+$ cells at hair placode stage are shown. GFP$^+$ cell lineages were determined at hair germ stage. **n**, Fate of basal and suprabasal cells in placodes of *Sox9-IRES-eGFP* reporter-derived dorsal skin explants. Fate of GFP$^+$ cells at the hair germ stage are shown. **o**, Lineage distribution of GFP$^+$ basal cells at hair germ stage. Cells grouped in the black bar in **n** were examined. **p**, Lineage-tracing strategy of *Sox9*$^+$ cells in ex vivo cultured dorsal skin derived from E12.5 *Sox9$^{creERt2/+}$;R26R-H2B-mCherry$^{fl/+}$;K14-H2B-eGFP* (top panel) and snapshot images of the culture (bottom panels). Yellow spots, one of tracked basal cell lineages; Cyan spots, one of tracked suprabasal cell lineages. 4-OHT, 4-hydroxytamoxifen. Scale bars, 50 μm. **q**, Fate of basal and suprabasal cells in the dorsal HF placode analysed by lineage-tracing with *Sox9-creER*. Fates of H2B–mCherry$^+$ cells at the hair germ stage are shown. Summarized data are shown in the left panel, and the data for corresponding replicate HFs are shown in the right panels. Two-sided Fisher's exact test was used. **r**, Lineage distribution of H2B–mCherry$^+$ basal cells at hair germ stage. Cells grouped in the black bar in **q** were examined. Summarized data are shown in the left panel, and the data for corresponding replicate HFs are shown in the right panels. Each value in the graph is the mean ± s.d. from three independent experiments, one or two HF each. Numbers of analysed cell lineages are summarized in Supplementary Table 2. See also 'Statistical analysis and reproducibility' in Methods and Source Data.

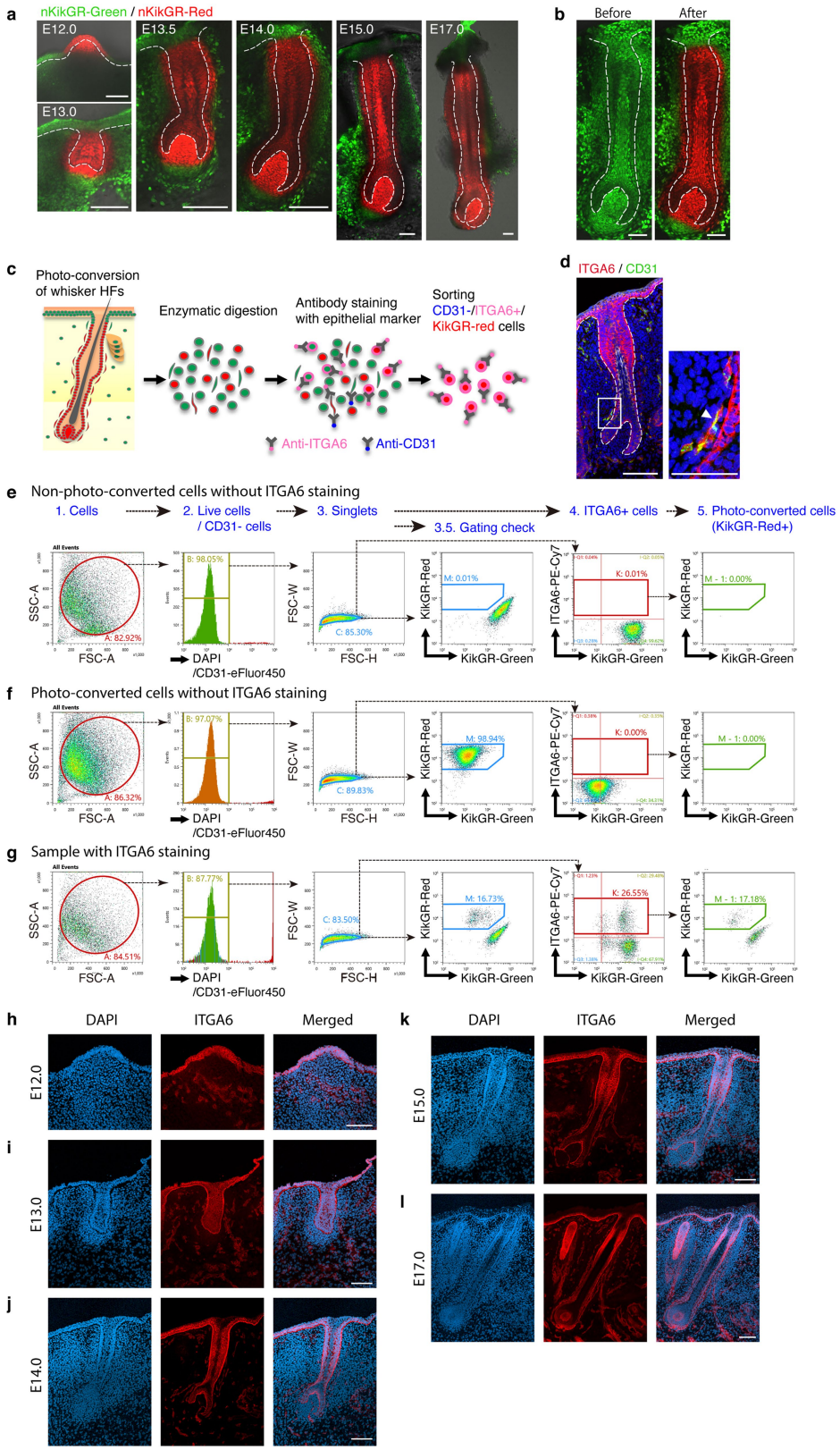

Extended Data Fig. 6 | See next page for caption.

Extended Data Fig. 6 | Cell sorting of photo-converted developing whisker HF epithelial cells. a, Photo-labelling of whisker HF epithelial cells in nKikGR mice at each embryonic stage. Scale bars, 50 μm. **b**, Single plane of E15.0 whisker HF showing the nKikGR signal intensities before and after the photo-conversion (Supplementary Video 9). Expression level of nKikGR varies between cells. There are two possible reasons for this: (1) the expression level of nKikGR varies for different cell types, and (2) the different mesenchymal tissue thickness of the explants around the whisker HFs affects the efficiency of detecting the fluorescent signals from the inside of the tissue. Despite this, the variation of nKikGR-green signal levels within the HF before photo-conversion closely correlates with the variation of nKikGR-red signal levels after photo-conversion, suggesting that the nKikGR signal was completely converted from green to red throughout the HF tissues (Supplementary Video 9). Scale bars, 50 μm. **c**, Experimental design for scRNA-seq of the developing whisker HF epithelium. **d**, Immunofluorescence staining of E14.0 whisker HF showed that the basal epithelial layer was marked by ITGA6^{+}CD31^{-} and that blood vessels in the mesenchyme were labelled by ITGA6^{+}CD31^{+} (arrowhead). Box shows magnified region (right). Scale bars, 50 μm. **e**–**g**, Isolation of photo-labelled whisker HF epithelial cells (E12.0–E17.0, DAPI^{-}CD31^{-}ITGA6^{+}KikGR-red^{+} cells; E11.5, DAPI^{-}CD31^{-}ITGA6^{+} cells) by flow cytometry. **h**–**l**, Immunolocalization of ITGA6 in developing whisker HFs. Whisker HFs at E12.0 (**h**), E13.0 (**i**), E14.0 (**j**), E15.0 (**k**) and E17.0 (**l**) were stained with an antibody against ITGA6, and sections were counterstained with DAPI. ITGA6 was detected in all basal epithelial cells of developing whisker HFs. Blood vessels in the dermis also were positive for ITGA6. Scale bars, 100 μm.

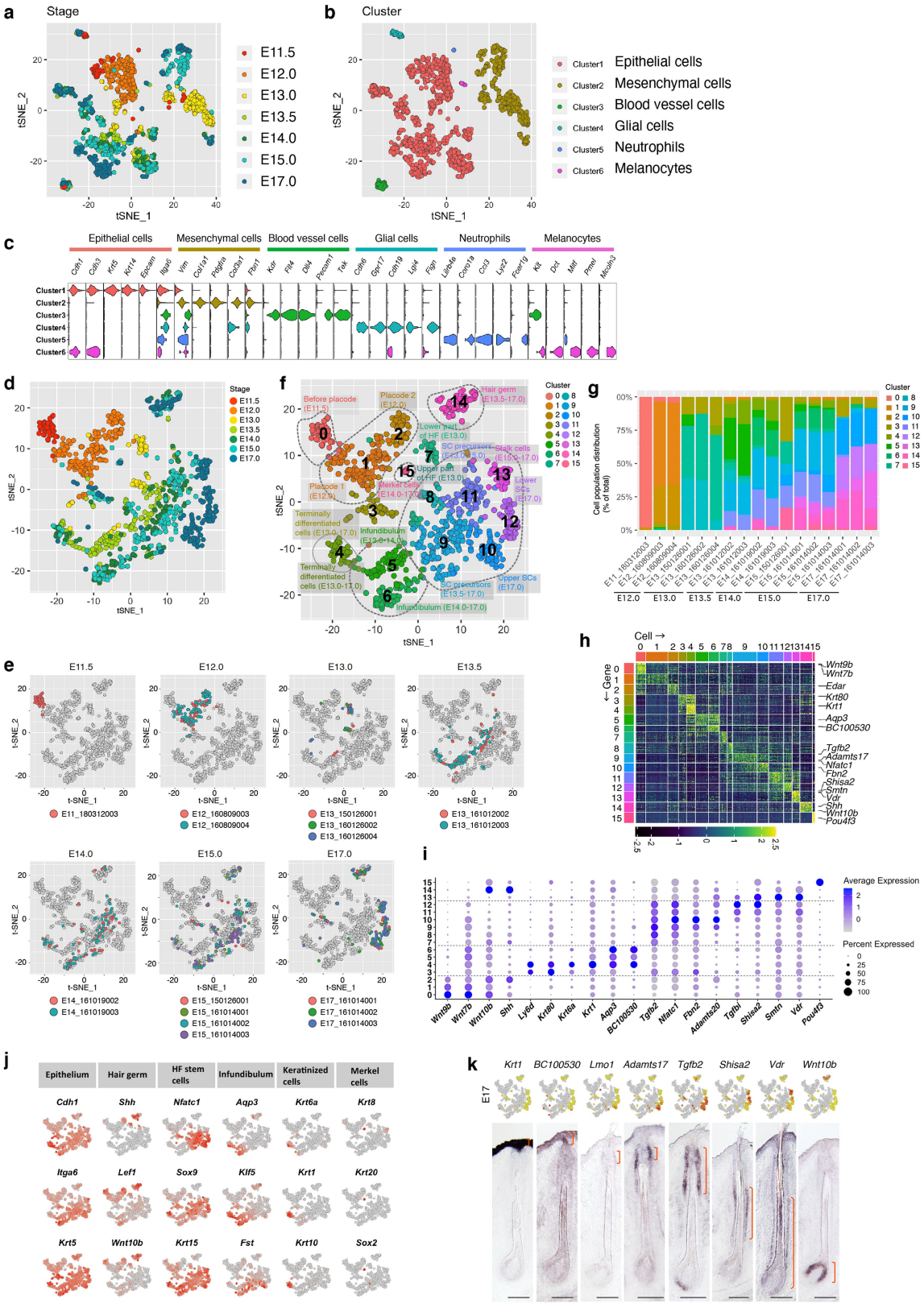

Extended Data Fig. 7 | See next page for caption.

Extended Data Fig. 7 | Spatial and temporal reconstruction of scRNA-seq data of the developing whisker HF epithelium. a, **b**, *t*-SNE plot visualizing scRNA-seq data for 1,614 single cells from developing whisker HFs (E11.5, 94 cells; E12.0, 276 cells; E13.0, 267 cells; E13.5, 181 cells; E14.0, 177 cells; E15.0, 350 cells; and E17.0, 269 cells). Cell populations were categorized by embryonic stage (**a**) and cell type (**b**). **c**, Violin plot showing the expression patterns of known lineage markers in each cluster. Colours refer to *t*-SNE clusters in **b**. **d**, Subclustering of whisker HF epithelial cells identified in **a**–**c**. *t*-SNE plot of 962 epithelial cells is coloured by embryonic stage. **e**, Low batch effects and high reproducibility of scRNA-seq data; scRNA-seq samples in this study consisted of cells from multiple batches: a plurality of plates and different dates and places of sampling, library preparation and sequencing. To investigate the batch effect caused by this technical handling, transcriptomes were divided into stages and projected onto the *t*-SNE plot corresponding to **d**. Grey spots in the *t*-SNE plot indicate all transcriptomes derived from E11.5–E17.0 epithelial cells. Cells derived from each stage were highlighted with different colours according to the batch of experiments. Cells from different batches were mixed stage-by-stage on the *t*-SNE plot and not clustered by batch. This suggests the low batch effects and high reproducibility of our scRNA-seq analysis. **f**, *t*-SNE plot in **d** is coloured by cluster annotations. **g**, Percentage cell cluster distribution per individual plate. Each plate derived from the same embryonic stage showed a similar distribution of the clusters. **h**, Heat map of the heterogeneity within and between clusters. **i**, Dot plot showing differentially expressed genes in each cluster identified in **f**. **j**, Expression of cell-type-specific marker genes projected onto the *t*-SNE plot in **d**. **k**, Expression of the marker genes projected onto the *t*-SNE plot are shown in the top panels, and the corresponding RNA ISH results are shown in the bottom panels. Grey spots in the *t*-SNE plot indicate all transcriptomes derived from E11.5–E17.0 epithelial cells. Only cells derived from E17.0 are highlighted and coloured according to relative expression levels of the markers. Brackets indicate the intended localization of ISH signals. Scale bars, 100 μm.

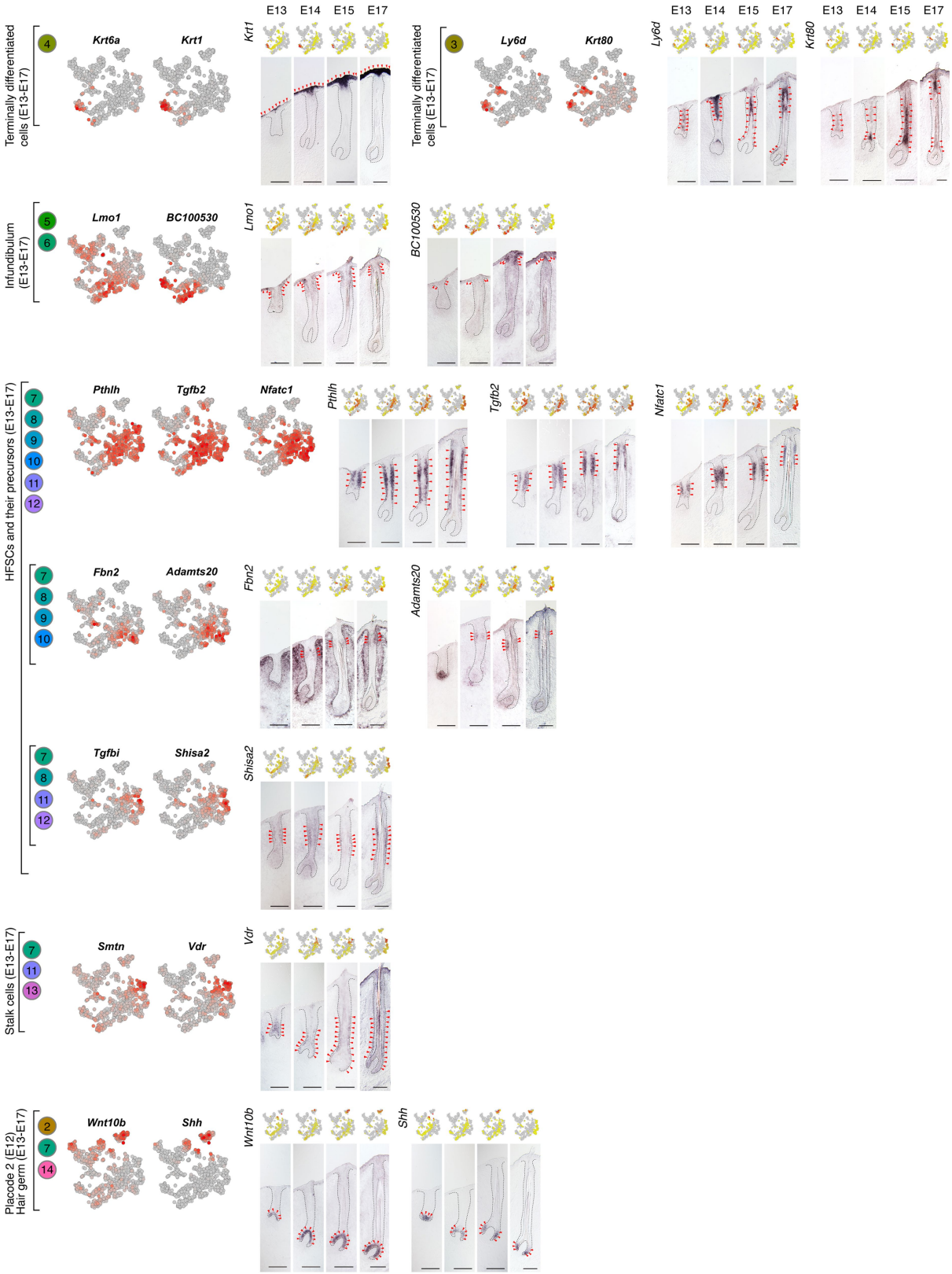

Extended Data Fig. 8 | See next page for caption.

Extended Data Fig. 8 | In vivo expression patterns of representative genes in each cell cluster of E13.0–E17.0 whisker HFs. Feature plots of characteristic differentially expressed genes in each cluster identified in Extended Data Fig. 7f are shown in the left panels. Feature plots divided by developmental stages of the whisker HFs (E13.0–E17.0) and the corresponding RNA ISH images are shown on the top and bottom right panels, respectively. Grey spots in the *t*-SNE plot indicate all transcriptomes derived from E11.5–E17.0 epithelial cells. Only cells derived from the indicated stage are highlighted and coloured according to relative expression levels of the indicated markers. Arrowheads indicate the intended localization of ISH signals. A cell cluster located at the lower part of the *t*-SNE plot (clusters 5 and 6) corresponded to the upper part of the HF, such as the infundibulum and junctional zone. A bulge SC marker (*Nfatc1*) was strongly expressed in cell clusters 7–12 located in the centre of the *t*-SNE plot. These clusters were divided into the upper and lower bulge regions, based on the expression pattern of each region marker (such as *Adamts20* and *Shisa2*). *Vdr* expression confirmed that clusters 7, 11 and 13 contained cells derived from the stalk region, the lower part of the HF. *Shh*-positive cells in cluster 14 were in the hair germ in vivo. These data indicated that cells were aligned from the bottom left to the top right on the *t*-SNE plot, reflecting the tissue architecture of the whisker HF. Scale bars, 100 μm.

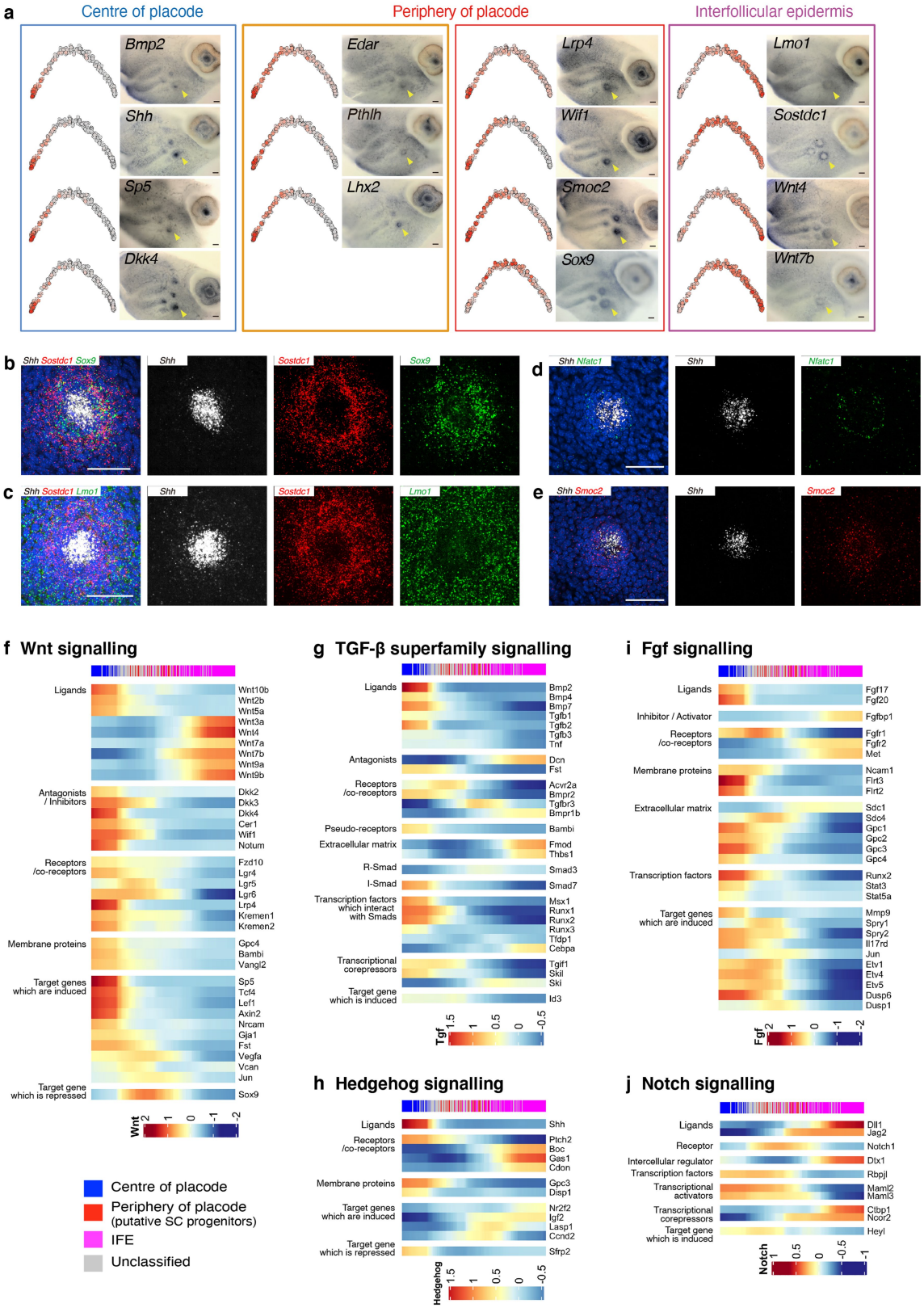

Extended Data Fig. 9 | See next page for caption.

Extended Data Fig. 9 | Pseudospace analysis of scRNA-seq data derived from E12.0 placode cells. a, In vivo expression patterns of representative genes in the pseudospace of E12.0 whisker HFs. Expression of the indicated marker genes projected onto the pseudospace are shown in the left panels, and the corresponding whole-mount RNA ISH results are shown in the right panels. Arrowheads indicate the intended localization of ISH signals. Scale bars, 100 µm. **b**–**e**, Expressions of indicated genes in an E14.5 primary dorsal HF placode were detected with whole-mount RNAscope fluorescent ISH. A merged image (left) and individual images are shown. Scale bars, 50 µm. **f**–**j**, Expression of genes related to signalling pathways in pseudospace of the hair placode. Genes involved in WNT (**f**), TGF, BMP and activin (**g**), Hedgehog (**h**), FGF (**i**) and Notch signalling (**j**) were selected from the KEGG database and the expression of the genes is represented in a heat map. Direct target genes of WNT and β-catenin signalling, including *Axin2* and *Tcf4*, showed high expression at the placode centre but suppression towards the IFE. However, the expression of Notch, FGF and TGF and BMP target genes, including *Heyl*, Etv genes and *Id3*, was more broadly elevated from the placode centre to the periphery. SHH target genes *Igf2* and *Ccnd2* were highly expressed from the periphery to the IFE regions. Thus, the placode basal epithelium forms gradients of signalling activities from the placode centre to the periphery, and the placode periphery is characterized, in part, as a $WNT^{low}BMP^{high}$ state, the characteristics of adult bulge SCs.

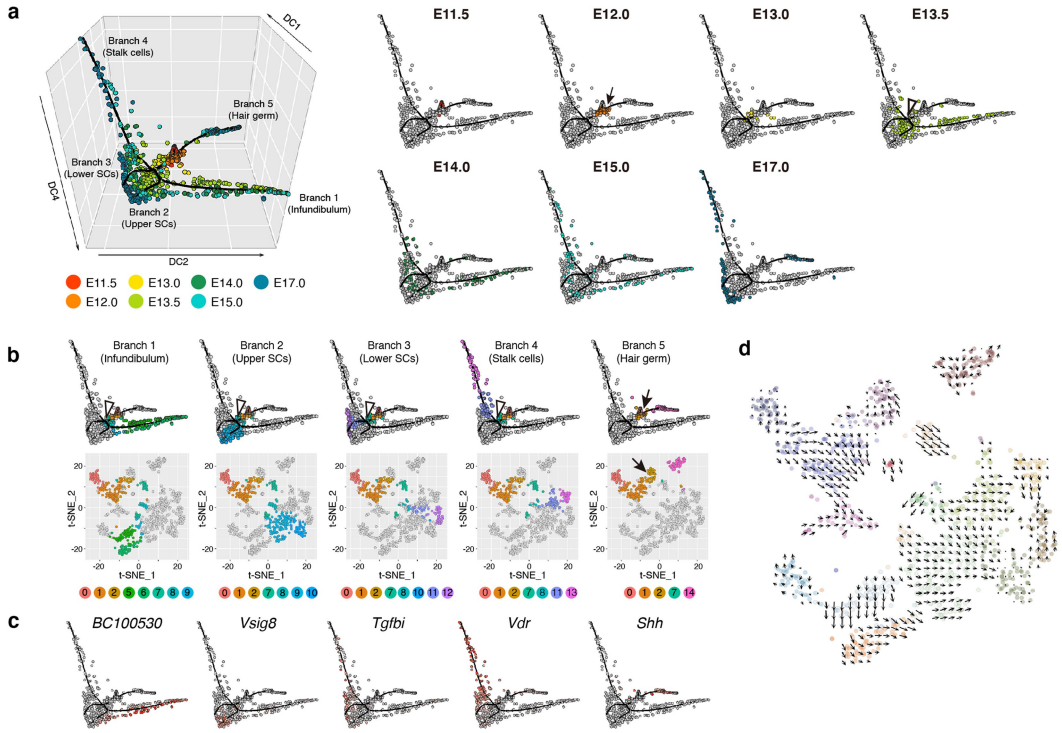

e

	ReactomeRA (p value < 0.03)	GO (p value < 0.03)	KEGG (p value < 0.03)
GC1	- Extracellular matrix organization - WNT ligand biogenesis and trafficking	- Frizzled binding - Integrin binding - Cell adhesion molecule binding	- Signalling pathways regulating pluripotency of stem cells - PI3K-Akt signalling pathway - Wnt signalling pathway - Proteoglycans in cancer
GC2		- Ubiquitin protein ligase binding - Unfolded protein binding	- DNA replication
GC3		- Metal ion transmembrane transporter activity - Cation channel activity	
GC4	- Cholesterol biosynthesis - Metabolism of steroids		- Steroid biosynthesis - Terpenoid backbone biosynthesis
GC5	- Glycolysis - Gluconeogenesis	- Transcription coregulator activity	- Carbon metabolism - Glycolysis/Gluconeogenesis
GC7	- M Phase - Cell Cycle Checkpoints	- Catalytic activity, acting on DNA	- DNA replication
GC8	- Keratinization	- Cell adhesion molecule binding - Calcium-dependent phospholipid binding	- Proteoglycans in cancer
GC9	- Laminin interaction - Cell-Cell communication - Cell junction organization	- DNA-binding transcription activator activity	- ECM-receptor interaction - Focal adhesion - TGF-beta signalling pathway
GC10	- Extracellular matrix organization	- Glycosaminoglycan binding - Heparin binding	- HIF-1 signalling pathway - Proteoglycans in cancer - Axon guidance - FoxO signalling - PI3K-Akt signalling pathway
GC11	- Signalling by receptor tyrosine kinases - Signalling by VEGF	- Protein tyrosine kinase activity - Growth factor binding	- PI3K-Akt signalling pathway - Axon guidance - Focal adhesion
GC12		- SMAD binding - I-SMAD binding - Beta-catenin binding	- Wnt signaling pathway - Basal cell carcinoma - Hippo signalling pathway - TGF-beta signalling pathway
GC13	- Keratinization - Formation of the cornified envelope	- DNA-binding transcription activator activity	

f

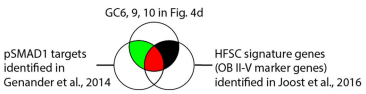

HFSC signature and pSMAD1 targets

GC6

2900026A02Rik, Abr, Acot1, Adrb2, Ankrd10, Anxa6, Arl8a, Asph, Atp1a1, Banp, Bmf, Ccdc3, Cldn23, Cldn8, Cacnb1, Cbr3, Cldsp2, Col7a1, Cpm, Dap, Ddit4, Dgkz, Egr2, Edn2, Fbln2, Frem2, Fryl, Foxp4, Gas1, Gm20554, Hjurp, Hpgds, H1f0, Irx2, Irx4, Itga4, Man2a2, Mfge8, Mgst1, Msi2, Neurl1b, Nfib, Nnt, Osbpl5, Papln, Pou2f3, Peg3, Ppp1r14c, Pthlh, Ptpru, Rbms3, Runx1, Rxra, Sema3e, Smoc2, Sox9, Srcin1, Ssfa2, Svil, Tgfb2, Tgfb3, Tmem40, Tnrc6a, Txndc16, Txnip, Uchl4, Vangl1, Zfp395, Zfp704

GC9

2610035D17Rik, Ankrd50, Aqp9, Arhgef5, Atp10d, Cav1, Cd63, Cited2, Col4a6, Cdh1, Cish, Cyr61, D930015E06Rik, Dsg2, Dst, Ehd2, Ehf, Emp3, Enah, Enox1, Fam83b, Far1, Flnb, Fos, Fosl2, Fst, Gsn, Has2, Hivep2, Hif, Hmces, Igfbp3, Irf2bp2, Itga6, Itgb4, Jup, Klk11, Krt15, Krt5, Lama3, Lamb2, Leng8, Lmna, Lrig1, Ltbp1, Malat1, Mctp2, Nfe2l2, P2ry1, Phlda1, Pitpnm3, Pou3f1, Ppp2r3a, Prkcd, Psat1, Pxdc1, Rgma, Sdcbp, Sec61a2, Slc12a2, Slc16a1, Slc2a1, Slc6a17, Smim3, Snai2, Snai3, Sox7, Tmsb4x, Tor2a, Traf3ip2, Tgif1, Wdr26

GC10

2010111I01Rik, 9930012K11Rik, Abca1, Ablim3, Adarb1, Adcy6, Aff3, Ampd3, Angptl2, Arap1, Ank, Ano6, App, Barx2, Bcl9l, Birc5, Btnf, Bmp7, Calml3, Cav2, Cbx6, Cdk5r1, Cebpb, Chdh, Cic, Cmpk2, Coml, Chd9, Clcn2, Clstn1, Col1a2, Col5a2, Creb5, Crim1, Ctbp2, Dkkl1, Dab2ip, Dclr1, Dhrs3, Eglf6, Ehf4, Ece1, Efna3, Esyn, Ephx1, Ercc5, Etl4, Fah, Fgfr1, Fzd7, Foxn3, Gas7, Gli1, Grm4, Golim4, Hif1a, Hs3st3b1, Ifitm3, Ifit2, Il17re, Ikbke, Irx1, Klhl42, Krt17, Krt24, Kctd15, Kdm4b, Krtcap3, Lgr4, Lhx2, Lrre4, Lif, Lima1, Lrp6, Ltbp2, Mal2, Mami2, Map1b, Mboat2, Mlf, Moxd1, Mtmr11, Mcf2l, Mdga1, Mertk, Mir1901, Mir23b, Mxd4, Nadk2, Ndufa4l2, Nedd9, Nfatc1, Nfia, Nrbp2, Nfil3, Nrcam, Nrtn, Palmd, Pcdh20, Pcsk6, Pdgfb, Pdzrn3, Pelo, Pfkfb3, Phyhip, Pik3ip1, Pkd1, Pla2g2f, Plekhg1, Plod1, Plxnb1, Pdlim2, Pfkp, Pik3r2, Plcg1, Plch2, Prdm11, Prdm1, Pik7, Ptprk, Ramp1, Ramp3, Rapgefl1, Rarg, Rasl10a, Repin1, Rgs11, Sdc3, Sec24d, Sema5a, Sertad4, Sh3rf1, Slc20a2, Slc29a1, Sash1, Sdc4, Sec14l1, Sema4c, Stxn3, Slc16a3, Slco4a1, Snx18, Socs3, Smim1, Sod1, Stom, Stx19, Tanc2, Tbx1, Tcf4, Tcp11l2, Thbs3, Timp3, Tle1, Tle3, Tnfrsf18, Tnk2, Tmem176b, Tnfrsf11b, Tns3, Trp73, Trps1, Ulk3, Vsig8, Vwa1, Vwa2, Wdr45, Wnk2, Ypel3, Zmiz1

Extended Data Fig. 10 | See next page for caption.

Extended Data Fig. 10 | Reconstruction of epithelial lineage diversification and SC induction. a, Timing of epithelial lineage divergence. Three-dimensional diffusion map showing pseudotemporally ordered whisker HF epithelial basal cells, related to Fig. 4c. Grey spots in the diffusion map indicate all transcriptomes derived from E11.5–E17.0 whisker HF epithelial basal cells. Cells derived from each stage are highlighted with different colours according to their embryonic stage. The arrow in the E12.0 diffusion map indicates the branching point of the hair germ lineage (branch 5). The open arrowhead in the E13.5 diffusion map indicates the branching point of infundibulum (branch 1), upper SCs (branch 2), lower SCs (branch 3) and stalk cells (branch 4). **b**, Cell clusters belonging to each trajectory are highlighted on the diffusion map (top panels) and *t*-SNE plot (bottom panels). Arrow and open arrowheads represent branching points. **c**, Expression of each lineage marker gene projected onto the diffusion map. **d**, RNA velocity field projected onto the *t*-SNE plot of epithelial cells (arrows represent the average RNA velocity). **e**, Selected terms of enrichment analysis associated with the gene categories identified in Fig. 4d. Only the gene list of gene cluster 6 raised no valid GO terms (P value < 0.03). **f**, HFSC signature genes and pSMAD1 targets in gene clusters 6, 9 and 10.

nature research

Corresponding author(s): Hironobu Fujiwara

Last updated by author(s): May 1, 2021

Reporting Summary

Nature Research wishes to improve the reproducibility of the work that we publish. This form provides structure for consistency and transparency in reporting. For further information on Nature Research policies, see Authors & Referees and the Editorial Policy Checklist.

Statistics

For all statistical analyses, confirm that the following items are present in the figure legend, table legend, main text, or Methods section.

n/a	Confirmed	
☐	☒	The exact sample size (*n*) for each experimental group/condition, given as a discrete number and unit of measurement
☐	☒	A statement on whether measurements were taken from distinct samples or whether the same sample was measured repeatedly
☐	☒	The statistical test(s) used AND whether they are one- or two-sided *Only common tests should be described solely by name; describe more complex techniques in the Methods section.*
☒	☐	A description of all covariates tested
☐	☒	A description of any assumptions or corrections, such as tests of normality and adjustment for multiple comparisons
☐	☒	A full description of the statistical parameters including central tendency (e.g. means) or other basic estimates (e.g. regression coefficient) AND variation (e.g. standard deviation) or associated estimates of uncertainty (e.g. confidence intervals)
☐	☒	For null hypothesis testing, the test statistic (e.g. *F*, *t*, *r*) with confidence intervals, effect sizes, degrees of freedom and *P* value noted *Give P values as exact values whenever suitable.*
☒	☐	For Bayesian analysis, information on the choice of priors and Markov chain Monte Carlo settings
☒	☐	For hierarchical and complex designs, identification of the appropriate level for tests and full reporting of outcomes
☒	☐	Estimates of effect sizes (e.g. Cohen's *d*, Pearson's *r*), indicating how they were calculated

Our web collection on statistics for biologists contains articles on many of the points above.

Software and code

Policy information about availability of computer code

Data collection

Image acquiring
- Olympus FV30S-SW (version 1.3.2.86)
- Olympus FV10-ASW (version 04.02)
- Olympus cellSens (version 1.18)
- Leica LAS X (version 3.5.5)
- Leica LAS (version 4.13)
- Zeiss Zen (version 2.3)
- Zeiss AxioVision (version 3.1.2.1)

Flow cytometry
- Sony SH800 Cell Sorter Software (version 2.1.5)

Data analysis

Software:
Image processing:
- Image J (version 1.51n)
- Python (version 3.7.4)
- Jupyter notebook (version 6.0.1)
- Bitplane AutoAligner (version 6.0.1)
- Bitplane IMARIS (version 9.2.1 and 8.4.2)
- Adobe photoshop (version 21.2.6)
- Adobe Illustrator (version 25.2.1)

Flow cytometry:
- Sony SH800 Cell Sorter Software (version 2.1.5)

scRNA-seq:
- Fastq-mcf (version 1.04.807)
- FastQC (version 0.11.5)
- HISAT2 (version 2.0.4)
- RseQC (version 2.6.4)
- Subread (version 1.5.0)
- Sailfish (version 0.10.0)
- R (version 3.4.3)
- Seurat (version 2.3.4 and 3.1.0)
- Python (version 3.7.4)
- Jupyter notebook (version 6.0.1)
- velocyto (version 0.17.15)
- Monocle (version 2.6.4)
- destiny (version 2.12.0)
- Slingshot (version 1.0.0)
- clusterProfiler (version 3.14.3)

Graph generation and data analysis:
- GraphPad Prism (version 9.0.2)
- ComplexHeatmap (version 2.2.0) with R
- ggplot2 (version 3.1.0) with R

Code:
Scripts used for scRNA-seq analysis is available at GitHub repository.
(https://github.com/Fujiwaralab/Morita_et_al_2021)

Source codes for analysis of the cell division orientation in live imaging data is available at GitHub repository.
(https://github.com/RIKEN-PHB/Morita-Paper-Spindle-Analysis)

For manuscripts utilizing custom algorithms or software that are central to the research but not yet described in published literature, software must be made available to editors/reviewers. We strongly encourage code deposition in a community repository (e.g. GitHub). See the Nature Research guidelines for submitting code & software for further information.

Data

Policy information about availability of data

All manuscripts must include a data availability statement. This statement should provide the following information, where applicable:

- Accession codes, unique identifiers, or web links for publicly available datasets
- A list of figures that have associated raw data
- A description of any restrictions on data availability

scRNA-seq data in this study have been deposited in the Gene Expression Omnibus (GEO) under accession code GSE147372.
(https://www.ncbi.nlm.nih.gov/geo/query/acc.cgi?acc=GSE147372)

Live imaging data in this study have been deposited in SSBD: repository.
(DOI: https://doi.org/10.24631/ssbd.repos.2020.06.002, http://ssbd.qbic.riken.jp/set/20200602/)

The mouse genome (mm10) is available at https://genome.ucsc.edu/.
Enrichr is available at https://maayanlab.cloud/Enrichr/.
KEGG PATHWAY Database is available at https://www.genome.jp/kegg/.

Source data for all main figures and Extended Data figures are provided with the paper.

Field-specific reporting

Please select the one below that is the best fit for your research. If you are not sure, read the appropriate sections before making your selection.

☒ Life sciences ☐ Behavioural & social sciences ☐ Ecological, evolutionary & environmental sciences

For a reference copy of the document with all sections, see nature.com/documents/nr-reporting-summary-flat.pdf

Life sciences study design

All studies must disclose on these points even when the disclosure is negative.

Sample size	Sample size was not predetermined, but determined to provide sufficient statistical power for analysis. Each replicate (HF)-derived dataset contained a large amount of cell lineage information.
Data exclusions	No data was excluded from the analysis.
Replication	Live imaging analysis was replicated using at least 3 independent biological samples (Precisely stated in the figure legends and Supplementaly

Replication	Tables). Representative micrographs came from at least two biological replicates.
Randomization	Experimental groups were determined by genotype. Both male and female embryos were used in experiments.
Blinding	In most of the experiments, no blinding method was possible as only one experimenter was performing the analysis.

Reporting for specific materials, systems and methods

We require information from authors about some types of materials, experimental systems and methods used in many studies. Here, indicate whether each material, system or method listed is relevant to your study. If you are not sure if a list item applies to your research, read the appropriate section before selecting a response.

Materials & experimental systems

n/a	Involved in the study
☐	☒ Antibodies
☒	☐ Eukaryotic cell lines
☒	☐ Palaeontology
☐	☒ Animals and other organisms
☒	☐ Human research participants
☒	☐ Clinical data

Methods

n/a	Involved in the study
☒	☐ ChIP-seq
☐	☒ Flow cytometry
☒	☐ MRI-based neuroimaging

Antibodies

Antibodies used

Imaging:
- mouse anti-NFATc1 Ab (1:100, sc-7294, Santa Cruz)
- goat anti-LHX2 Ab (1:50, sc-19344, Santa Cruz)
- rabbit anti-SOX9 Ab (1:50, sc-20095, Santa Cruz)
- rabbit anti-SOX9 Ab (1:1000, ab185966, Abcam)
- rabbit anti-Ki67 Ab (1:100, ab15580, Abcam)
- Alexa555-labeled mouse anti-Krt15 Ab (1:200, Watt lab)
- PE-labeled rat anti-CD49f (Integrin alpha6) Ab (1:50, 12-0495-83, eBioscience,)
- Goat anti-P-cadherin (CDH3) Ab (1:40, AF761, R&D)
- Rabbit anti-Stearoyl-CoA desaturase (SCD1) Ab (1:100, HPA012107, Sigma-Aldrich)
- HCS LipidTOX™ Deep Red Neutral Lipid Stain (1:200, H34477, Invitrogen)
- Mouse anti-Actin, α-Smooth Muscle (SMA) Ab [1A4] (1:800, A2547, Sigma)
- Rabbit anti-SOX2 Ab (1:200, ab97959, Abcam)
- Rabbit anti-KRT17 Ab (1:100, ab53707, Abcam)
- Alexa Fluor® 546-labeled Mouse anti-pan-Cytokeratin Ab [AE13] (1:50, sc-57012 AF546, Santa Cruz)
- Guinea pig anti-KRT82 Ab (Ready-to-use, 70022, Progen)
- Guinea pig anti-KRT75 Ab (Ready-to-use, 70022, Progen)
- Alexa Fluor® 488-labeled Mouse anti-GATA3 Ab [L50-823 (RUO)] (Ready-to-use, 560163, BD Biosciences)
- Alexa Fluor® 546-labeled Mouse anti-Trichohyalin Ab [AE15] (1:50, sc-80607 AF546, Santa Cruz)
- DyLight 488-labeled Mouse anti-KRT14 Ab [LL002] (1:100, NBP2-34675G, Novus Biologicals)
- Rabbit anti-Keratin6 Ab (1:500, PRB-169P, Covance)
- Goat anti-TRP2 Ab (1:100, sc-10451, Santa Cruz)
- Rabbit anti-Nephronectin Ab (1:200, Watt lab)
- DAPI (1:2000, D523, Doujin Kagaku)
- Alexa Fluor® 488-conjugated Goat anti-Mouse IgG1(1:1000, A21121, Molecular Probes)
- Alexa Fluor® 555-conjugated Donkey anti-Goat IgG (H+L) (1:1000, A21432, Molecular Probes)
- Alexa Fluor® 647-conjugated Donkey anti-Goat IgG (1:1000, A21447, Molecular Probes)
- Alexa Fluor® 488-conjugated Donkey anti-Rabbit IgG (1:1000, A21206, Molecular Probes)
- Alexa Fluor® 647-conjugated Donkey anti-Rabbit IgG (1:1000, A31573, Molecular Probes)
- Alexa Fluor® 647-conjugated Goat anti-Guinea Pig IgG (H+L) (1:1000, A21450, Molecular Probes)
- Alexa Fluor® 488-conjugated Donkey anti-Rat IgG (H+L) (1:1000, A21208, Molecular Probes)
- Alexa Fluor® 488-conjugated Rat monoclonal anti-Mouse IgG2a heavy chain [SB84a] (1:1000, ab172324, Abcam)

Flow cytometry:
- eFluor450-labeled anti-mouse CD31 (1:100, 48-0311-82, eBioscience)
- PE-Cy7-labeled anti-human/mouse CD49f (1:100, 25-0495-82, eBioscience)
- DAPI (1:2000, Doujin Kagaku)

The antibodies used are also shown in Supplementary Table 4.

Validation

The antibodies used were validated by previous works and /or the manufacturer. The company website contains validation data for each antibody. All antibodies were tested in house using cryosectioned mouse skin tissue samples and sample staining with only secondary antibody were used as a negative control.

- mouse anti-NFATc1 Ab (1:100, sc-7294, Santa Cruz)
https://www.scbt.com/p/nfatc1-antibody-7a6?productCanUrl=nfatc1-antibody-7a6&_requestid=3193865

- goat anti-LHX2 Ab (1:50, sc-19344, Santa Cruz)
https://www.scbt.com/p/lhx2-antibody-c-20?requestFrom=search

- rabbit anti-SOX9 Ab (1:50, sc-20095, Santa Cruz)
https://www.scbt.com/p/sox-9-antibody-h-90?requestFrom=search

- rabbit anti-SOX9 Ab (1:1000, ab185966, Abcam)
https://www.abcam.com/sox9-antibody-epr14335-78-ab185966.html

- rabbit anti-Ki67 Ab (1:100, ab15580, Abcam)
https://www.abcam.com/ki67-antibody-ab15580.html

- Alexa555-labeled mouse anti-Krt15 Ab (1:200, Watt lab)
Cell . 2011 Feb 18;144(4):577-89. doi: 10.1016/j.cell.2011.01.014.
https://www.sciencedirect.com/science/article/pii/S0092867411000158?via%3Dihub

- PE-labeled rat anti-CD49f (Integrin alpha6) Ab (1:50, 12-0495-83, eBioscience)
https://www.thermofisher.com/antibody/product/CD49f-Integrin-alpha-6-Antibody-clone-eBioGoH3-GoH3-Monoclonal/12-0495-83

- Goat anti-P-cadherin (CDH3) Ab (1:40, AF761, R&D)
https://www.rndsystems.com/products/mouse-p-cadherin-antibody_af761

- Rabbit anti-Stearoyl-CoA desaturase (SCD1) Ab (1:100, HPA012107, Sigma-Aldrich)
https://www.sigmaaldrich.com/catalog/product/sigma/hpa012107?lang=en&region=US

- HCS LipidTOX™ Deep Red Neutral Lipid Stain (1:200, H34477, Invitrogen)
https://www.thermofisher.com/order/catalog/product/H34477#/H34477

- Mouse anti-Actin, α-Smooth Muscle (SMA) Ab [1A4] (1:800, A2547, Sigma)
https://www.sigmaaldrich.com/catalog/product/SIGMA/A2547?lang=en&region=US

- Rabbit anti-SOX2 Ab (1:200, ab97959, Abcam)
https://www.abcam.com/sox2-antibody-ab97959.html

- Rabbit anti-KRT17 Ab (1:100, ab53707, Abcam)
https://www.abcam.com/cytokeratin-17-antibody-cytoskeleton-marker-ab53707.html

- Alexa Fluor® 546-labeled Mouse anti-pan-Cytokeratin Ab [AE13] (1:50, sc-57012 AF546, Santa Cruz)
https://www.scbt.com/p/pan-cytokeratin-antibody-ae13?productCanUrl=pan-cytokeratin-antibody-ae13&_requestid=3196756

- Guinea pig anti-KRT82 Ab (Ready-to-use, 70022, Progen)
- Guinea pig anti-KRT75 Ab (Ready-to-use, 70022, Progen)
https://www.progen.com/anti-hair-keratin-sample-set.html

- Alexa Fluor® 488-labeled Mouse anti-GATA3 Ab [L50-823 (RUO)] (Ready-to-use, 560163, BD Biosciences)
https://www.bdbiosciences.com/us/applications/research/t-cell-immunology/th-2-cells/intracellular-markers/cell-signalling-and-transcription-factors/human/alexa-fluor-488-mouse-anti-gata3-l50-823/p/560163

- Alexa Fluor® 546-labeled Mouse anti-Trichohyalin Ab [AE15] (1:50, sc-80607 AF546, Santa Cruz)
https://www.scbt.com/p/trichohyalin-antibody-ae15?requestFrom=search

- DyLight 488-labeled Mouse anti-KRT14 Ab [LL002] (1:100, NBP2-34675G, Novus Biologicals)
https://www.novusbio.com/products/cytokeratin-14-antibody-ll002_nbp2-34675g

- Rabbit anti-Keratin6 Ab (1:500, PRB-169P, Covance)
https://www.biolegend.com/en-us/products/purified-anti-mouse-keratin-6a-antibody-11459?GroupID=GROUP26

- Goat anti-TRP2 Ab (1:100, sc-10451, Santa Cruz)
https://www.scbt.com/p/trp2-antibody-d-18?requestFrom=search

- Rabbit anti-Nephronectin Ab (1:200, Watt lab)
Cell . 2011 Feb 18;144(4):577-89. doi: 10.1016/j.cell.2011.01.014.
https://www.sciencedirect.com/science/article/pii/S0092867411000158?via%3Dihub

- Alexa Fluor® 488-conjugated Goat anti-Mouse IgG1(1:1000, A21121, Molecular Probes)
https://www.thermofisher.com/antibody/product/Goat-anti-Mouse-IgG1-Cross-Adsorbed-Secondary-Antibody-Polyclonal/A-21121

- Alexa Fluor® 555-conjugated Donkey anti-Goat IgG (H+L) (1:1000, A21432, Molecular Probes)
https://www.thermofisher.com/antibody/product/Donkey-anti-Goat-IgG-H-L-Cross-Adsorbed-Secondary-Antibody-Polyclonal/A-21432

- Alexa Fluor® 647-conjugated Donkey anti-Goat IgG (1:1000, A21447, Molecular Probes)

https://www.thermofisher.com/antibody/product/Donkey-anti-Goat-IgG-H-L-Cross-Adsorbed-Secondary-Antibody-Polyclonal/A-21447

- Alexa Fluor® 488-conjugated Donkey anti-Rabbit IgG (1:1000, A21206, Molecular Probes)
https://www.thermofisher.com/antibody/product/Donkey-anti-Rabbit-IgG-H-L-Highly-Cross-Adsorbed-Secondary-Antibody-Polyclonal/A-21206

- Alexa Fluor® 647-conjugated Donkey anti-Rabbit IgG (1:1000, A31573, Molecular Probes)
https://www.thermofisher.com/antibody/product/Donkey-anti-Rabbit-IgG-H-L-Highly-Cross-Adsorbed-Secondary-Antibody-Polyclonal/A-31573

- Alexa Fluor® 647-conjugated Goat anti-Guinea Pig IgG (H+L) (1:1000, A21450, Molecular Probes)
https://www.thermofisher.com/antibody/product/Goat-anti-Guinea-Pig-IgG-H-L-Highly-Cross-Adsorbed-Secondary-Antibody-Polyclonal/A-21450

- Alexa Fluor® 488-conjugated Donkey anti-Rat IgG (H+L) (1:1000, A21208, Molecular Probes)
https://www.thermofisher.com/antibody/product/Donkey-anti-Rat-IgG-H-L-Highly-Cross-Adsorbed-Secondary-Antibody-Polyclonal/A-21208

- Alexa Fluor® 488-conjugated Rat monoclonal anti-Mouse IgG2a heavy chain [SB84a] (1:1000, ab172324, Abcam)
https://www.abcam.com/rat-monoclonal-sb84a-mouse-igg2a-heavy-chain-alexa-fluorreg-488-ab172324.html

Flow cytometry:
- eFluor450-labeled anti-mouse CD31 (1:100, 48-0311-82, eBioscience)
https://www.thermofisher.com/antibody/product/CD31-PECAM-1-Antibody-clone-390-Monoclonal/48-0311-82

- PE-Cy7-labeled anti-human/mouse CD49f (1:100, 25-0495-82, eBioscience)
https://www.thermofisher.com/antibody/product/CD49f-Integrin-alpha-6-Antibody-clone-eBioGoH3-GoH3-Monoclonal/25-0495-82

- DAPI (1:2000, Doujin Kagaku)
https://www.dojindo.co.jp/products/D523/

Animals and other organisms

Policy information about studies involving animals; ARRIVE guidelines recommended for reporting animal research

Laboratory animals	Mus musculus was used as an animal model and the strains used are shown as below. - C57BL/6 mice (purchased from SLC, Inc.) - FVB/NJcl mice (purchased from CLEA Japan) - K14-H2B-EGFP #67 mice (generated in this study; RIKEN BDR, Acc. No. CDB0544T-1) - K14-H2B-EGFP #406 mice (generated in this study; RIKEN BDR, Acc. No. CDB0544T-2) - R26R-CAG-nKikGR (RIKEN BDR, Acc. No. CDB0312K) - R26-CAG-nKikGR (RIKEN BDR, Acc. No. CDB0318K) - FVB-Tg(KRT14-rtTA)F42Efu/J [K14-rtTA] (The Jackson Laboratories, JAX stock #008099) - STOCK Tg(tetO-HIST1H2BJ/GFP)47Efu/J [TetO-H2B-EGFP] (The Jackson Laboratories, JAX stock #005104) - B6.Cg-Tg(FucciG1)#596Bsi [Fucci-red] (RIKEN Bioresorce, RBRC No. RBRC02707) - R26R-H2B-mCherry (RIKEN BDR, Acc. No. CCDB0204K) - R26-H2B-mCherry mice (RIKEN BDR, Acc. No. CDB0239K) - R26R-Lyn-Venus mice (RIKEN BDR, Acc. No. CDB0219K) - KRT5-cre mice (kindly provided by Dr. Jose Jorcano in CIEMAT-CIBERER, Madrid, Spain) - B6.129S7-Sox9<tm1(cre/ERT2)Haak> [Sox9-CreERT2] (RIKEN Bioresorce, RBRC No. RBRC05522) - B6;129S4-Sox9tm1.1Tlu/J [Sox9-IRES-EGFP] (The Jackson Laboratories, JAX stock #030137) - B6(Cg)-Tyrc-2J/J (The Jackson Laboratories, JAX stock #000058) All mice were bred to albino mice: FVB/NJcl mice or B6(Cg)-Tyrc-2J/J to avoid imaging interference from melanin deposition. Male and female embryos (E11.5, E12.0, E12.5, E13.0, E13.5, E14.0, E14.5, E15.0, E15.5, E16.5, E17.0, E17.5, E19.5 and P5) were used in this study. All animals were housed in SPF (specific pathogen free) animal facilities. Mice were maintained in a 12h-light/12h-dark cycle and temperatures of 18–23C with 40–60% humidity.
Wild animals	No wild animals were used.
Field-collected samples	No field-collected samples were used.
Ethics oversight	All experimental procedures were approved by the RIKEN Center for Biosystems Dynamics Research (BDR) Institutional Animal Care and Use Committee. All mouse care and handling complied with the ethics guidelines of the RIKEN BDR.

Note that full information on the approval of the study protocol must also be provided in the manuscript.

Flow Cytometry

Plots

Confirm that:

☒ The axis labels state the marker and fluorochrome used (e.g. CD4-FITC).

☒ The axis scales are clearly visible. Include numbers along axes only for bottom left plot of group (a 'group' is an analysis of identical markers).

☒ All plots are contour plots with outliers or pseudocolor plots.

☒ A numerical value for number of cells or percentage (with statistics) is provided.

Methodology

Sample preparation	The photo-converted whisker follicles at each developmental stage (E12.0-E17.0) were dissociated into single cell suspension as below. The dissected tissues were washed in ice-cold PBS and then immersed in 0.25% Trypsin solution (Nacalai) for 5 hrs at 4 °C. Subsequently, the tissues were treated twice at 37 °C for 5–30 min in 0.25% trypsin and 100U/ml DNaseI (Sigma), and then dissociated into single cells by gentle pipetting. The dissociated cells were spun down, resuspended in PBS supplemented with 0.5% BSA, and filtered through a 40-µm mesh. The cells were adjusted to 1×10^6 cells/ml and stained with eFluor450-labeled anti-mouse CD31 (1:100, 48-0311-82, eBioscience), PE-Cy7-labeled anti-human/mouse CD49f (1:100, 25-0495-82, eBioscience) and DAPI (1:2000, Doujin Kagaku). To isolate epithelial cells just before the placode formation, the maxillary prominences of E11.5 embryos were dissected, directly treated with trypsin and stained with the above antibodies without photo-labelling since there are no distinguishable structure leading to hair placode formation.
Instrument	SH800 cell sorter (Sony)
Software	Sony SH800 Cell Sorter Software (version 2.1.5) was used to collect samples and analyse.
Cell population abundance	Sample collection was performed with index sorting. The purity of the sample was always assessed in sorting experiments (>98%).
Gating strategy	Our gating strategy is as below. E12.0-E17.0 whisker follicles used for scRNA-seq: DAPI/CD31-negative, CD49f-positive, photo-converted nKikGR positive (Extended Data Fig. 6e-g) E11.5 epidermal cells of the maxillary prominences used for scRNA-seq: DAPI/CD31-negative, CD49f-positive Doublets were excluded using a FSC-H/FSC-W gating strategy. Unstained samples and single staining controls were always used to determine the gating area.

☒ Tick this box to confirm that a figure exemplifying the gating strategy is provided in the Supplementary Information.